Title: CA1 Engram Cell Dynamics Before and After Learning

Authors: Amy Monasterio[1], Caitlin Lienkaemper[2,4], Siria Coello[3], Ryan Senne[1], Gabriel K. Ocker[2,4], Steve Ramirez[2,3,5,6] and Benjamin B. Scott[2,3,5,6]

[1]Graduate Program for Neuroscience,
[2]Center for Systems Neuroscience,
[3]Department of Psychological and Brain Sciences,
[4]Department of Mathematics and Statistics,
[5]Center for Neurophotonics, Boston University, Boston, MA, USA
[6]Equal Contribution

Keywords
Hippocampus, engram, learning, immediate-early gene, spontaneous activity, memory
Correspondence: bbs@bu.edu and dvsteve@bu.edu

Summary

A fundamental question in neuroscience is how memory formation shapes brain activity at the level of neuronal populations. Recent studies of hippocampal 'engram' cells—neurons identified by learning-induced immediate early gene (IEG) expression—propose that these populations form the cellular substrate for memory. Previous experimental work suggests that cells are recruited into engrams via elevated intrinsic excitability and that learning drives coactivity among these cells to support retrieval. Despite this, an understanding of how engram dynamics evolve across learning and recall remains incomplete. Here, we combined activity-dependent genetic tagging with longitudinal two-photon calcium imaging to track CA1 engram population dynamics before and after fear conditioning. Our results reveal that engram activity is modulated by intrinsic dynamics, behavioral state, and stimulus-cued reactivation. First, spontaneous activity during quiet rest–up to two days before Fos expression–predicted future engram membership, consistent with the idea that intrinsic dynamics bias engram allocation. In parallel, we found sequential activity during locomotion recruited both engram and non-engram cells, but that engram cells were less modulated by velocity after contextual fear conditioning. Surprisingly, after fear conditioning, we didn't find changes in the average spontaneous activity rates or correlations of CA1 engram cells. However, within the engram population, we identified a subset of cells that increased their spontaneous correlations after fear learning, specifically during quiet rest. Furthermore, we used a trace fear conditioning paradigm to show that CS presentation drove elevated activity and increased correlations amongst engram cells, demonstrating learning-dependent reactivation. Finally, computational modeling of CA3-CA1 circuit dynamics demonstrated that a network with strong excitatory-inhibitory balance, capable of CA3-driven reactivation, is consistent with our experimental results. Together, these results show that memory formation reshapes engram population dynamics across spontaneous states, behavior, and recall.

Introduction

While decades of research have established the central role of the hippocampus in episodic memory formation, the precise mechanisms by which neuronal populations are selected to participate in individual memories are still undefined. A rich body of literature suggests that learning drives plasticity within populations of neurons activated by experience.[1,2] This plasticity involves a dynamic series of changes in gene expression and synaptic connectivity which are thought to drive corresponding changes in activity patterns at the population level. Together these changes in gene expression, connectivity, and activity are thought to constitute a neurophysiological memory trace and are often referred to as a memory engram.[2]

Historically, two complementary approaches have been used to characterize such engrams. First, in vivo population recording of cells active during memory tasks and spatial navigation has been fundamental in understanding the coding properties of hippocampal neurons.[3] Second, 'engram-tagging' studies in the past decade have used IEG expression, such as Fos or Arc, to identify populations of neurons and to demonstrate their necessity and sufficiency in driving the behavioral expression of memory.[4–6] While numerous cases of artificial

manipulation of engram-tagged populations have driven a suite of behaviors ranging from fear recall (i.e., freezing[5,6]), approach,[7,8] and motivated behaviors,[9,10] surprisingly less is known about how patterns of activity in engram assemblies change with learning.

Bridging the gap between cellular mechanisms and behavioral memory expression requires linking fast, intracellular events such as gene expression and spontaneous activity changes to slower, systems-level outcomes like post-learning population dynamics and behavioral phenotypes. Although a few studies have recorded hippocampal engram-tagged cells during navigation after *Fos*-based tagging—revealing distinct spatial selectivity and ensemble dynamics compared to non-engram cells—how the activity of engram populations transforms across the course of memory formation remains poorly understood.

Two complementary hypotheses inform how engram populations relate to memory formation. The allocation hypothesis proposes that pre-existing cellular excitability influences the recruitment of cells during novel experiences.[13,14] This idea is supported by numerous experiments that manipulate cellular excitability levels *before* learning. In addition, IEG-based engram-tagging research has converged on the idea that coactivity among engram cells emerges *after* learning and therefore comprises a physiological correlate for memory.[15–17] This hypothesis is supported by recent work identifying structural and synaptic properties of engram cells in vitro–namely, that engram cells show a higher level of connectivity between each other compared to non-engram cells.[17–19]

To evaluate these hypotheses, we used a combination of activity-dependent genetic tagging, longitudinal calcium imaging, and computational modeling to characterize spontaneous activity in CA1 engram populations before and after learning. First, we discovered that spontaneous activity during periods of rest before learning was informative for engram allocation at a time point up to two days before immediate-early gene expression. In contrast, engram cells were less modulated by velocity than non-engram cells, though both populations participated in behavioral timescale sequences during head-fixed locomotion. These findings indicate that intrinsic dynamics and locomotion both influence engram dynamics.

Surprisingly, when evaluating engram cell activity, we did not observe changes in engram cell activity rates or their average correlation after contextual learning. However, we did observe a subset of engram cells that increased their pairwise correlations during rest, after contextual fear learning. Furthermore, we utilized trace conditioning and a CS-mediated recall paradigm to describe the effects of memory cues on CA1 engram dynamics. CS presentation resulted in increased population activity that was greater in engram cells across trials, in addition to increased correlations between engram cells. These reactivation dynamics were consistent with network simulations incorporating strong excitatory-inhibitory balance and CA3 reactivation.

Overall, our results bridge in vivo cellular dynamics with Fos-expressing populations, thus revealing both pre-existing and state-dependent physiological properties of memory-engram cells across learning and memory.

Results

Two-photon imaging of engram and non-engram populations

To record engram dynamics over time, we used tetTag virus constructs to identify engram cells and transgenic Thy1-GCaMP6f mice to record calcium activity in dorsal CA1 (Figure 1A). During imaging, head-fixed mice were free to walk on a rotating disk and we measured spontaneous locomotion. We used a custom kinematic headplate[20] to register the head across sessions and reliably record calcium activity (GCaMP) and tet-driven mCherry in the same populations across days (Figure 1B, Supplementary Figure 2A). In a 405 x 405 µm field of view we observed an average of 177 +/- 6 spontaneously active neurons. We were able to track the same cells across days and observed a turnover in the pool of active cells registered across 4 days (Figure 1F). 55.0% +/- 1.7% of cells from Day 0 remained active on Day 4, while 45.0 % +/- 1.7% percent of cells turned over from Day 0 to Day 4. Tet-driven mCherry expression was used to identify putative engram cells (Figure 1C-D, Supplementary Figure 1, Methods).

Spontaneous activity in engram cells before and after learning

To assess how the activity of engram cells changes over time, we recorded CA1 populations before and after learning. Day 0 baseline spontaneous activity was recorded in a population of CA1 pyramidal neurons prior to Fos-tagging (Figure 1A). On Day 2 mice either underwent a 3-shock contextual fear conditioning protocol (FC, n=8, Supplementary Figure 3E) or remained in the homecage (HC, n=8), a neutral experience that still drove Fos-tagging. Dox was replaced on Day 2 to close the window for mCherry labeling, and a second imaging session of spontaneous activity took place on Day 4 (Figure 1A-B).

We classified cells as either engram or non-engram based on their Day 4 mCherry expression (Figure 1C-D, see Methods). Therefore, we define ‘engram’ here, as cells identified by their Fos-expression in a given tagging window (Figure 1A-C). Approximately ~30% of spontaneously active cells were mCherry+ and therefore classified as engram cells (Figure 1G). This proportion was similar across FC and HC mice, and between in vivo imaging and histology (Supplementary Figure 3A). In addition to cells active on both days we defined two other classes of cells: those only active on Day 0 (OUT cells, Figure 1F) and cells only active on Day 4 (IN cells, Figure 1F). In both FC and HC mice, we observed an increased number of mCherry+ cells that became active on D4 (Figure 1F, IN cells FC p=0.0007, HC p=0.045), compared to those that dropped out of the population from D0 (OUT Cells). This effect was stronger in the FC mice, suggesting that fear learning may promote cells to join the population of spontaneous activity cells in CA1 (Figure 1F).

Increased activity prior to tagging biases Fos-tagging, independent of experience

With this approach, we first sought to test the first prediction of the allocation hypothesis, namely if spontaneous activity before learning could predict engram tagging. To do this, we deconvolved calcium activity and calculated event rates for each cell on Day 0 such that event rates were weighted by the size of transients (Methods). We separated cells into deciles within each animal, from least to most active (Supplementary Figure 5A-B). Cells in different deciles were distributed in space throughout the FOV (Supplementary Figure 5C). We observed a significant positive correlation between a cell's activity decile on Day 0 and the likelihood it would be Fos-tagged (Figure 2A, $R^2 = 0.82$, $p = 0.00033$.). Interestingly, this effect was seen in both FC and HC groups (Figure 2B-C, FC $R^2 = 0.64$, $p = 0.0048$, HC $R^2 = 0.77$, $p = 0.0009$). Spontaneous activity during rest, but not during locomotion, was correlated with engram tagging (Figure 2D-F, Rest: $R^2 = 0.8$, $p = 0.00049$; Run: $R^2 = 0.31$, $p = 0.09$). These results suggest that increased activity at a time point up to 48 hours before Fos-tagging correlates with allocation, independent of which experience was tagged (i.e. aversive footshock or neutral homecage).

To validate these results, and since this analysis averaged information across cells and animals, we also used hierarchical Bayesian generalized linear models to test the relationship between Day 0 activity and likelihood of engram tagging (HB-GLM; see Methods). This analysis revealed a strong relationship between Day 0 activity during rest and tagging, consistent with previous analysis (Supplementary Figure 5D-G). More specifically, GLMs that included resting state activity rates demonstrated improved predictive performance against a model only based on running state activity rates, or a null model (Supplementary Figure 5F-G).

Together, these analyses of Day 0 activity rates provide converging evidence that spontaneous activity in engram cells during rest is predictive of future engram recruitment. This supports the idea that internal, pre-experience dynamics, particularly during rest, are a critical signature of engram allocation.

Engram cells remain more active during rest across conditions

We next asked if engram cells maintained their higher activity across days, and if this changed after fear learning. To address this, we identified active cells across both Day 0 and Day 4 and compared their mean calcium event rate across each session. Interestingly, engram cells had higher activity rates at both timepoints in both FC and HC mice (Figure 3A-B), in agreement with previous recordings of engram cell activity in CA1.[11,12, 25] We saw no increase in activity amongst engram cells from Day 0 to Day 4 in either group of mice, but found a Group x Session interaction (Supplementary Figure 4A-B, $p = 0.001$ Linear Mixed Effects Model). To control for variability in locomotion (Supplementary Figure 4C) and the general increase in rates caused by more locomotion (Supplementary Figure 4D), we recalculated event rates during separate periods of locomotion and periods of quiet rest (Figure 3B-C). We observed a modest decrease in event rate across both groups during resting activity on Day 4 ($p = 0.026$) and not running ($p = 0.85$) (Figure 3B-C). Interestingly, the increased activity in engram cells was only significant during rest periods

173 (Figure 3C, p = 0.004) and not run periods (Figure 3D, p = 0.145). Overall, these results suggest
174 that Fos-identified engram populations display higher levels of spontaneous activity that was more
175 accurately detected during periods of quiet rest compared to running.

176 Engram and non-engram cells are differentially modulated by 177 behavior state

178 Previous studies have identified spatially or temporally patterned sequences of hippocampal
179 activity that are associated with navigation, memory and locomotion.[26–28] These sequential
180 dynamics are thought to organize memories by providing biological scaffolds for space and time
181 that are relevant to behavior. We asked how engram and non-engram cells may contribute to
182 such dynamics. Examination of population dynamics from CA1 with Rastermap[29] revealed
183 sequential patterns of activity that were consistently associated with locomotion bouts activity
184 (Figure 3D). While both engram and non-engram cells participated in these sequences, a larger
185 proportion of sequentially active cells were non-engram cells (Figure 3E, 2-Way RM-ANOVAs
186 Population x Day, FC Population, p = 0.0096 HC Population p = 0.0005). Furthermore, population
187 activity of non-engram cells was more correlated with velocity (Figure 3F), an effect that was
188 statistically significant in FC mice only *after* learning (p = 0.005 FC, D4 engram vs non-engram).
189 These data suggest that while engram and non-engram populations participate in locomotion
190 related sequences, engram populations are less modulated by locomotion after fear learning.

191 A subset of engram cells increase their spontaneous correlations 192 after fear learning

193 A key prediction of many engram-tagging studies is that after learning, engram neurons have
194 stronger synaptic connectivity that drives their co-activity.[2,30] To test this prediction, we calculated
195 pairwise Spearman correlations for all pairs of cells on Day 0 and Day 4 (Figure 4A), such that
196 each pairwise correlation was between engram cells (E/E pairs), engram and non-engram cells
197 (E/N) or non-engram cells (N/N). After fear learning, the mean pairwise correlations across
198 populations did not demonstrate any significant differences, however, there was a non-significant
199 decrease in engram correlations in FC mice (Figure 4B, Linear Mixed Effects Model Group x
200 Population, p = 0.07. This was driven by changes in running behavior across days in FC mice
201 (Supplementary Figure 4C), and disappeared when calculating rest and run correlations while
202 controlling for time (Figure 4C). We explored the potential mechanisms underlying this lack of
203 engram correlations after learning, by implementing a spiking network model of CA3-CA1 (see
204 Methods), based on a Hebbian increase in synaptic weights between engram-units in both regions
205 (Supplementary Figure 8A). Initially, increasing synaptic weights in our model led to increases in
206 pairwise correlations between engram units (Supplementary Figure 8B). However, the addition of
207 homeostatic plasticity and strong global excitatory-inhibitory balance throughout the network, was
208 sufficient to mask this mean change in engram correlations, similar to our in vivo data
209 (Supplementary Figure 8C). This points to E/I balance as a potential circuit mechanism that is
210 consistent with our observed spontaneous activity here.
211

We next focused only on significantly correlated cell pairs by applying significance thresholds to our pairwise correlations. Correlated cell-pairs were thresholded such that only pairs with significant correlations on both days were analyzed (p-values less than thresholds ranging from 0.05 to 10e-5, Supplementary Figure 6A-B). In addition, to account for time lags between pairs of cells, we repeated these correlations on binned traces of the deconvolved activity using a range of time bins (0.27 to 4 seconds). We found that during rest, in FC mice, significantly correlated E/E and E/N cell pairs became more highly correlated after fear conditioning compared to N/N pairs, (Figure 4D-E). This effect was not observed in HC mice (Figure 4F-G, Linear mixed-effects model, Group x Population interaction, FC x E/E p = 0.002, FC x E/N p =0.0005). Conversely, correlations during running did not show these effects (Supplementary Figure D-G).

In summary, these data suggest that a subset of existing engram correlations increase after learning in a state dependent manner. Consistent with our activity rate results, these analyses show that, under conditions of spontaneous activity, changes in engram cell correlations are revealed during states of quiet rest.

Imaging engram dynamics during cued reactivation after trace fear conditioning

While our data thus far demonstrate that spontaneous activity dynamics evolve across memory formation, we next sought to explore how memory retrieval states could impact activity in engram populations. To do this, we tracked engram population activity in a new group of mice that underwent trace fear conditioning followed by imaging engram population activity during the presentation of the tone conditioned stimulus (i.e. CS) (Figure 5A). Similar to our first experiment, baseline activity was measured on Day 0 and dox was removed. While off dox, trace fear conditioning (TFC) training consisted of 3 trials of a 2.8 kHz tone (20s), followed by a 20s trace period, and an aversive foot shock. In a separate cohort of mice, we ensured that this tone CS served as an effective fear cue to induce a fear response in a distinct, neutral environment (Supplementary Figure 3F). After training, mice were again imaged on Day 4 for a recall session. After 10 minutes of baseline recording, 10 trials of the CS were presented, once every 100 seconds for the remainder of the session (Figure 5A). This approach enabled us to record CA1 engram cells during a baseline period after learning, as well as during cue-evoked (CS) activity.

First, we replicated our result from our spontaneous recordings (Figure 2A-B) – we found that during the baseline period, engram cells demonstrated higher activity rates, especially during rest periods (Supplementary Figure 7A-B). Upon CS-presentations, we observed increased locomotion in head-fixed mice, which often began a new running bout from rest (Figure 5B-C, p = 0.006, Supplementary Figure 7C), consistent with a learned US-CS association (but see Discussion). Importantly, the CS presentation drove increased activity in both engram and non-engram cells (2Way RM ANOVA Main Effect of Epoch, p = 0.0001), however, more-so in engram cells (Figure 5E, paired t-test, p = 0.003). While activity rates varied across trials, engram cells consistently demonstrated higher activity than non-engram cells (Figure 5F, 2Way RM ANOVA, p = 0.015). We still found locomotion-related sequences during these times, similar to before CS presentation (Supplementary Figure 7C). These data reveal that CS presentation increases

activity in both engram and non-engram cells, but that engram cells demonstrate stronger re-activation during the CS.

Our reactivation data was supported by our spiking network model, when we simulated upstream engram reactivation in CA3 (Supplementary Figure 8D). In this simulation, when a subset of CA3 engram units received excitatory input, mimicking the recall stimulus (Supplementary Figure 8E-F). As a result, downstream CA1 engram units increased their spiking and pairwise correlations (Supplementary Figure 8G-H), similar to our in vivo data (Figure 5D-E). Interestingly, our network model was able to recapitulate these results when targeted stimulation of excitatory engram cells was paired with a nonspecific disinhibitory input (Supplementary Figure 8E-F). Overall, our imaging findings and model simulation are consistent with numerous IEG-experiments showing engram-reactivation at recall and represent novel in vivo evidence that engram cells are strongly reactivated during cue-mediated memory recall.

Finally, to see how CS presentation affected correlated activity between engram cells, we calculated the maximum cross correlation between cell pairs within a 2s time lag during the recall session after CS presentation began (Figure 5G). Compared to the baseline period before stimulus presentations (Figure 5F), during tone presentations and ITI periods, engram pairs (E/E) demonstrated increased relative correlations compared to engram/non-engram (E/N, $p = 0.07$) and non-engram/non-engram pairs (Figure 5F-G, Linear Mixed Effects Model, Main effect of N/N $p = 0.003$). In addition, our spiking network model, mimicked these effects, with engram-engram units displaying higher correlations when CA3 engram excitatory units were driven (Supplementary Figure 8H). These results suggest that increased correlated activity amongst engram cells compared to other populations can be driven by CS mediated retrieval.

Discussion

We investigated the dynamics of Fos-tagged engram cells in CA1 before and after fear learning using an intersectional approach that combined in vivo imaging of cell population and activity dependent tagging. Overall, our experiments reveal that engram calcium dynamics are modulated by pre-existing hippocampal dynamics, locomotion, fear learning, and CS-mediated retrieval.

First, we observed that activity up to two days before fear conditioning was predictive of Fos-tagging (Figure 2). This spontaneous activity was most informative about cell identity when including periods of quiet rest, a state in which engram cells displayed increased calcium activity in spontaneous recordings (Figure 2, Figure 3A-C). We also found that sequential hippocampal activity during locomotion recruited both engram and non-engram cells, however, engram cells were less strongly modulated by velocity, a relationship that emerged after fear conditioning (Figure 3D-F). Next, we discovered that correlations in spontaneous activity during rest periods increased in a subset of highly correlated engram neurons after fear learning, an effect that was learning-specific (Figure 4C-F). Finally, recording during CS-cued reactivation demonstrated increased activity (Figure 5D-E) and correlations (Figure 5F-G) amongst engram cells following memory reactivation. Together, these results reveal several novel aspects of the underlying activity of Fos-tagged engram populations as it relates to behavior and memory.

Allocation revealed in spontaneous dynamics

Our finding that increased spontaneous activity prior to experience is predictive of IEG-tagging further supports the popular allocation model of engram formation.[13,14] Previous evidence for the allocation model came initially from manipulation studies, in which over-expression of CREB or optogenetic stimulation of cells prior to learning increased their likelihood of reactivation, during memory recall.[14,25–29] While there is wide support for this model of engram formation, several aspects of the allocation model have yet to be characterized. First, it remains unclear whether these intrinsic fluctuations in the hippocampus are cell autonomous, such that each cell cycles independently through periods of high and low excitability, or whether pre-existing networks fluctuate together.[25–27,29,] Secondly, the timescales of these intrinsic fluctuations are unknown. On the one hand shorter timescales on the order of minutes to hours have been observed to contain physiological activity predictive of memory allocation [26,29,30] , whereas other studies propose that intrinsic fluctuations that can exist across days, as a mechanism for linkage of fear memories across days, but not weeks.[31,32,37] More recently, a study used in vivo imaging to track direct endogenous fluctuations in calcium dynamics prior to IEG-tagging.[29] They found that cells with higher levels of activity several hours prior to fear conditioning were more likely to undergo IEG-tagging, which we believe resonates with our findings that such higher levels of activity can appear even days prior to a learning event. While they reported that increased excitability was only detectable in tagged engram cells within the same day as learning, it is important to note they normalized calcium activity within cells across days. In comparison, here we compared the engram- to non-engram population activity, which does not prevent the possibility of within-engram changes the day of learning. Taken together, evidence across multiple groups points to the existence of heterogeneous dynamics, including both short and long timescale intrinsic fluctuations. Such heterogeneity could be rooted in various biological underpinnings including, but not limited to, intrinsic CREB expression, receptor recycling and homeostatic structural-functional changes.

Fos ensembles for aversive and neutral experiences

In our analyses of baseline activity, we found the relationship between prior spontaneous activity and engram-tagging existed in both aversive (FC) or neutral (HC) conditions (Figure 2, Day 0). This suggests that increased spontaneous activity predicts Fos-tagging, regardless of experience valence. In prior work studying their behavioral relevance, FC-tagged Fos cells drove freezing while neutral-tagged cells did not.[5,7,8,38,39] While this approach focused on the role of valenced experiences in mediating the ability of Fos-tagged ensembles to drive behavior, the physiological similarities or lack thereof between neutral or fear-related Fos assemblies remained unmeasured. Studies measuring the structural properties of engram cells, however, show increased spine densities and size on neutral and pre-existing connectivity between Arc-tagged cells days before gene expression.[18] These findings highlight 1) importance of continued investigation of learning-related changes in IEG-populations compared to cells involved in neutral or homecage experiences, and 2) the need for experience-based behavioral controls in engram-tagging experimental designs. Our results here suggest that some features of IEG-ensembles

may decouple behavioral experience from physiology of engram cells by identifying aspects of Fos-ensemble function that are independent of experience or valence.

State-dependent dynamics in engram populations

Interestingly, our finding that increased spontaneous activity was important for future IEG-tagging was state-dependent, and strongest during rest-period activity. This observation is particularly relevant given that the hippocampus displays highly structured dynamics such as sharp-wave ripples (SWRs), replay and preplay during rest and offline periods.[33–36] Interestingly, there is preliminary evidence that Fos-tagged CA1 pyramidal cells are strongly modulated by SWRs (bioRxiv). Such structured activity is thought to support successful encoding and consolidation of episodic experiences, and contribute to memory guided decision-making.[33,37] While we were unable to identify such fast-timescale sequential dynamics in this approach, one interesting future direction would be to investigate whether engram cell assemblies display reliable and specific fast-timescale sequences of firing prior to learning and tagging, and whether these sequences change after learning.

While differences in engram vs non-engram dynamics were most evident in spontaneous activity during rest periods, during run periods both engram and non-engram cells participated in sequences of activity (Figure 3D). However, non-engram cells were more strongly correlated with velocity, which became significant in FC after fear conditioning (Figure 3E-F). This learning-induced difference aligns with previous evidence that driving FC-tagged engram cells in CA1 promotes freezing, as after fear learning engram cells were less-correlated with velocity (Roy et al., 2022, Ryan et al, 2015, Vetere et al., 2017). These behavioral-timescale sequences of activity are similar to previous reports that found repeated sequences of distance-coding in head-fixed mice with no visual cues (Villette et al, 2015). In addition, during spatial navigation in virtual reality, Fos-positive place cells also participated in sequential place field activations (Pettit et al 2022). These findings suggest that Fos-ensembles can participate in both spontaneous activations during rest and locomotion during navigation, which supports their involvement in both types of hippocampal activity.

Correlated activity in engram cells after learning

Our experiments also revealed specific post-learning changes in functional correlations between CA1 engram cells. While we did not detect widespread increases in spontaneous correlated engram activity after learning in head-fixed mmice, wedid discover a subset of highly-correlated engram cells that strengthened their co-activity (Figure 4A, 4D). Our results are in agreement with a previous study in which a decrease in average correlation after learning was observed, in addition to the emergence of a subset of highly correlated cells after fear learning (Rajesupathy, et al 2015). Interestingly, this effect extended to engram/non-engram correlations, which is consistent with a recent connectomics study that also found increased synaptic strength both within engram/engram and engram/non-engram connectivity from CA3 to CA1 (Uytiepo et al., 2025). Finally, these increases were state-dependent as this effect was not seen in run-state activity. These findings point to several novel insights: first, subsets of highly correlated engram cells demonstrate state- and learning-dependent changes across a days-long timescale in

spontaneous activity. Second, the consequences of plasticity amongst hippocampal engram populations on circuit dynamics cannot be solely explained by Hebbian potentiation, since these correlations were state-dependent and also strengthened between engram and non-engram cells. Finally, the fact that this increase was only evident in cells with some degree of coupling is consistent with the idea that pre-existing functional relationships may shape memory ensembles and be stabilized during learning (Mocle, Attardo). Future studies and analytical approaches may be aimed to identify these 'sub-ensembles' within IEG-labeled populations (Ghandour et al 2019), and characterize how their existence or stability are changed by learning.

Lastly, aside from spontaneous correlated activity, we also sought to investigate how reactivation of the fear representation influenced engram cell activity. We discovered engram-specific reactivation during CS presentation after trace fear conditioning, as CS presentations drove higher activity and correlations between engram cells compared to non-engram cells (Figure 5G). Together these findings indicate that CA1 engram populations can be reactivated by the presentation of a fear-CS, reinforcing their participation in memory retrieval, consistent with Fos-reactivation studies.[51] These data represent a novel, in vivo, demonstration of Fos-tagged engram cells reactivating to a CS during cued memory recall. Future studies may use this approach to characterize different aspects of memory cue encoding, during learning or retrieval in Fos networks—such as stimulus identity, coding stability and remapping across extinction or new learning.

Somewhat surprisingly, we did not detect sequential dynamics at stimulus onset or offset tiling the trace period, though the velocity modulated sequences still existed (**Error! Reference source not found.**). These results are consistent with a recent report that did not detect sequential activity in CA1 during head-fixed trace fear conditioning.[52] This study did however find that subsets of neurons still encoded CS identity at longer timescales, which is consistent with what we report here, as cross correlations between engram cells were present on the timescale of seconds (Figure 5. Engram activity during cued reactivation). This contrasts with other learning tasks in which 'time-cells' fired in reliable sequences in a task-dependent manner.[53–55] These tasks generally incorporate shorter stimulus or delay durations, compared to trace fear conditioning, in addition to using appetitive learning. This discrepancy may indicate that longer-timescale delays in aversive conditioning may recruit distinct neural activity patterns, though additional experiments are warranted to explicitly investigate this.

Limitations of the study

A key issue with many IEG-tagging studies lies in the difficulty of estimating the onset and duration of the tagging window. This problem is particularly acute with the tet-Tag system when doxycycline is administered in the animal's diet. We chose this system for its wide use in engram-tagging studies and the evidence that cells labeled with this system can drive memory behaviors. However, several unknowns limit the precise knowledge of onset and duration of tagging including the timing of the animal's last meal, the half-life of doxycycline (which could be variable across animals), the concentration of doxycycline needed to suppress gene expression, the possibility that concentrations may be lower in the brain[45], and the half-life of tTA-protein. Previous studies have suggested that the tagging window opens within 24 hours of food removal[5] however finer timescale measurements have not been performed to our knowledge. Moreover, we point out that

there may be high variability from animal to animal based on individual and strain differences[46] in the rate of doxycycline metabolism and the timing and amount of dox food consumed. Future studies could more precisely measure the onset and duration of doxycycline-dependent gene expression. Alternatively, future studies could shift to more recently developed tagging systems with greater temporal precision.

Other studies have utilized the TRAP2[29,47] system as it labels a smaller proportion of CA1 during a shorter time window, around 5% of spontaneously active cells[29] which is much lower than we observed here. While we are not aware of any studies that have described genotype-, dose-, or brain-region specific differences in TRAP2 tagging levels, these methodological differences must be considered when comparing across studies. Furthermore, the amount of CA1 cells labeled with Fos-dependent approaches range from 5-30%, highlighting a need for systematic comparison of activity-dependent strategies[48,49] with endogenous Fos levels, which is both brain-region and experience dependent. In addition to the TRAP2 system, newly developed methods that utilize faster timescale light-dependent systems include Cal-Light[50], scFLARE[51,52] and FLiCRE[53] which permit genetic tagging of cells on a seconds-timescale. However, care should be taken when selecting methods as these more temporally restricted tools rely on light activation for tagging that may preclude simultaneous photoexcitation for functional imaging. Thus, employing more temporally restricted techniques combined with experimental designs in which behavior is monitored longitudinally, can be done systematically in future studies to reveal the mechanisms surrounding memory allocation.

Conclusion

Our study reveals fundamental mechanisms of hippocampal engram cell physiology and their predictive relationship with IEG-expression. To successfully integrate these approaches, it is crucial to combine measurements of population physiology over time with IEG-tagging techniques and measure endogenous activity. Towards that end, here we combined in vivo imaging, IEG-tagging, behavior and simple spiking models to conclude that more excitable cells were biased IEG-tagging, identify conditions of correlated activity amongst engram cells after learning, and suggest future avenues for mechanistic investigations of engram population activity from a circuit perspective. Our results are consistent with emerging literature and support a framework in which engrams are shaped by both existing hippocampal dynamics, behavior states and memory formation.

Acknowledgements:
We would like to thank Jack Giblin, Kivilcim Kilic and the BU Neurophotonics Center for their training and support, and Joseph Zaki for helpful discussion of analyses. Denise Cai and Michael Hasselmo provided valuable comments. AM was supported by an NSF NRT award and an NIH DSPAN award. BBS was supported by a Young Investigator award from the BBRF and by a SEED grant from the BU Neurophotonics Center. CL was supported by a Center for Systems Neuroscience Distinguished Postdoctoral Fellowship. This material is based upon work supported by an NIH Early Independence Award DP5 OD023106-01, NIH Transformative Award, Air Force Office of Scientific Research (AFOSR; FA9550-21-1-0310), the Ludwig Family Foundation, the

Pew Scholars Program in the Biomedical Sciences, the Chan-Zuckerberg Initiative, and the Center for Systems Neuroscience and Neurophotonics Center at Boston University.

Author contributions:
Experiment design: AM, SR, BBS
Mouse imaging & behavioral experiments: AM, SC
Data analysis: AM, SC, RS
Spiking model design & simulations: CL, GKO
Manuscript writing: AM
Manuscript editing: AM, CL, BBS, SR, GKO

Declaration of Interest: The authors declare no competing interests.

Methods

Key Resources Table

Reagent or Resource	Source	Identifier
Experimental models: Organisms/strains		
C57BL/6J-Tg(Thy1-GCaMP6f)GP5.17Dkim/J	The Jackson Laboratory	Strain 025393
Bacterial and virus strains		
AAV9-c-fos-tTA-BGHpa	UMass Vector Core	Custom Ordered
AAV9-TRE-mCherry	UMass Vector Core	Custom Ordered
Chemicals, peptides and recombinant proteins		
Doxycycline diet (40 mg/kg)	Bio-Serv	Custom ordered dose
Software and algorithms		
Python 3.10	Python Software Foundation	https://www.python.org/
Arduino	Arduino	https://www.arduino.cc/
CellReg	Sheintuch et al. 2017 218/9/24 11:24:00 AM	https://github.com/flatironinstitute/CaImAn

CaImAn	Giovanucci et al 2019 [578/9/24] 11:24:00 AM	https://github.com/zivlab/CellReg
ImageJ (FIJI)	National Institutes of Health	https://fiji.sc/
FreezeFrame4	Actimetrics, Lafayette, IN	https://actimetrics.com/

Experimental Methods

Animals & Handling

Transgenic Thy1-GCaMP6f[58] (C57BL/6J-Tg(Thy1-GCaMP6f)GP5.17Dkim/J, Jackson Labs #025393, 16-24 weeks) were group housed with littermates prior to experiment start and given food and water *ad libitum.* The animal vivarium was maintained on a 12:12-hour light cycle (0700-1900). Following surgery, mice were single-housed to prepare for imaging experiments. All subjects were treated in accord with protocol 201900084 approved by the Institutional Animal Care and Use Committee (IACUC) at Boston University. Prior to imaging experiments, mice were habituated for 5 days to head-fixation.

Stereotaxic Surgery & Window Implantation

For all surgeries, mice were initially anesthetized with 3.0% isoflurane inhalation during induction and maintained at 1.5%–2% isoflurane inhalation through stereotaxic nose-cone delivery (oxygen 1L/min). Ophthalmic ointment (Systane) was applied to the eyes to provide adequate lubrication and prevent corneal desiccation. The hair on the scalp above the surgical site was removed using Veet hair removal cream and subsequently cleaned with alternating applications of betadine solution and 70% ethanol. 2.0% lidocaine hydrochloride was topically applied as local analgesia prior to midsagittal incision using an 11 blade scalpel of the scalp skin to expose the skull. A 0.1 mg/kg intraperitoneal (IP) dose of buprenorphine was administered at the beginning of surgery. A unilateral craniotomy was performed with a .5mm drillbit for viral injection. A 10 uL Hamilton syringe with an attached 33-gauge beveled needle was slowly lowered to the coordinates of dorsal CA1: -2.0 AP, +1.5ML -1.5 DV. 400 nL of 1:1 cocktail of AAV9-cFos-tTA/AAV9-TRE-mCherry (UMass Vector Core, titer $1x10^{13}$ GC/mL) was injected at a rate of 100 nL/min. The needle was allowed to rest at the injection site for 1-2 min prior to and after injection. Incisions were sutured closed using 4/0 Non-absorbable Nylon Monofilament Suture (Matrix Wizard). Following surgery, mice were injected with a 5 mg/kg intraperitoneal (IP) dose of ketoprofen. They were placed in a recovery cage with a heating pad until fully recovered from anesthesia. Histological assessment verified spread of dorsal CA1 viral targeting.

Seven to ten days later, a second surgery was performed to implant a hippocampal window for two-photon imaging. Prior to surgery, dexamethasone (3 mg/kg) was administered IP to aid brain swelling and inflammation. A 3mm craniotomy was created centered at the site of viral injection. Dura was peeled back with a bent 27-gauge needle tip. Cortical tissue washed with sterile saline while aspirated using constant suction attached to 25-30 gauge needle tips. Tissue was aspirated down to white matter and corpus callosum fibers were carefully removed, leaving alveolar fibers

intact. Blood was constantly removed via aspiration and absorption with saline-soaked hemostatic collagen sponge (Goodwill Hemosponge Absorbable Gelatin Sponge).

For the window implant, a 3mm diameter, 1.5mm deep stainless steel circular cannula (Ziggy's Tubes & Wires) was affixed to a 3 mm glass coverslip (#1 thickness, Thomas Scientific 1217N66) using UV curable optical adhesive (Norland). The cannula window was lowered carefully into the craniotomy site and Vetbond was used to adhere the edges of the cannula to the skull. The scalpel and drillbit was used to hatch the skull surface for best adhesion to the headplate. A custom stainless steel kinematic headplate[20] was affixed to the skull with the cannula centered using Metabond (Parkell). Mice were allowed to recover at least 1 week prior to handling & imaging took place 2 weeks after surgery.

Two-photon Imaging

All imaging was performed on a Bruker Ultima Investigator in Prairie View (v5.4). Excitation was delivered with a tunable Ti:Sapphire laser (Insight X3, Spectra Physics) at wavelengths of 920nm or 1040 nm and a primary dichroic (700 SP) split excitation and fluorescence light and a 770 SP IR blocker ensured no laser power reached the PMTs. On each imaging day, image series were collected at a frame rate of 30Hz with resonant galvos and resolution of 512x512 pixels. All imaging was with a 16x Nikon (3.0 mm, 0.8 NA) water immersion objective. Laser power was controlled with an electro-optic modulator (Conoptics 305-105-20) and post objective power ranged from 10-80 mW and did not exceed 100 mW. Emitted fluorescence was split into red and green channels with an emission filter cube set (565 LP dichroic, 525/70 for the green channel and 595/50 for red) and detected with two PMTs, for green (Hammamatsu H10770PB-40) and red (Hammamatsu H10770PB-50) channels. For recording spontaneous activity, 1-2 FOVs were recorded per animal for 22 minutes on Day 0 and Day 4 at 920nm. 1 FOV was excluded from 5 out of 12 mice due to either unreliable cell registration or resonant galvo image artifacts. For recording dual color GCaMP/TRE-mCherry expression, the same FOVs were recorded for ~1 minute (2000 frames) at a wavelength of 1040 nm. All dual color data was recorded at identical power settings on Day 0 and Day 4 in order to characterize mCherry fluorescence change across days.

During imaging mice were placed on a custom rotating disk that enabled them to locomote. A kinematic headplate and mount system was custom designed to ensure reliable registration of imaging FOV day to day and allowed for locomotion.[20] The imaging apparatus consisted of the kinematic mount held in place with ½" Thorlabs posts above a horizontal running disk. The rotating acrylic disk was 7" in diameter and a soft rubber adhesive was used to provide the mice traction for running on the disk. The center of the disk was screwed into an adjustable collar (McMaster Carr 9410T1) and mounted on a rotary encoder (US Digital H1-5000-IE-D) to measure running. A custom arduino script was used to record and synchronize image acquisition with running data from the disk. Wheel data was recorded in 13 of 16 mice for Figures 1-4 (CFC/HC mice) and for all mice in Figure 5 (TFC mice).

Running behavior

To collect locomotion data, an arduino script was used to record timestamped positional data from the mouse's running disk. Timestamps were aligned to imaging frames by interpolating wheel positional data with known frame times from Prairie View xml metadata files. To determine

552 walking/running epochs, a velocity threshold of 1 cm/s was imposed to select for frames to
553 account for spurious movement of the running disk. Run epochs were selected requiring that the
554 animal be greater than one for longer than 0.5 seconds and rest epochs were selected requiring
555 the animal to be still for at least 0.5 seconds.
556
557 *Fear Conditioning Tagging and Behavior*
558 Prior to surgeries, mice were placed on a special diet of doxycycline chow (40 mg/kg, BioServ).
559 When dox chow was removed (end of D0), this opened the window for activity-dependent viral
560 labeling during the tagging period. For tagging, HC mice remained untouched in the home cages,
561 while FC mice were placed in a conditioning chamber with plexiglass walls and a grid floor (17.78
562 cm L × 17.78 cm W × 30.48 cm H; Coulbourn Instruments) for a 7-minute conditioning session.
563 Grid floors were connected to precision shockers and delivered a series of three footshocks (2 s,
564 1.0 mA intensity) at times 200s, 280s and 360s. Immediately after fear conditioning, the
565 doxycycline diet was replaced in all mice cages immediately after tagging and mice remained on
566 doxycycline diet for the duration of the imaging protocol (until after Day 4). Dox was removed after
567 the conclusion of imaging sessions to allow full expression of tet-driven mCherry and check for
568 injection spread (data not shown). For fear conditioning, video data were collected via overhead
569 cameras (Computar) that interface with FreezeFrame (Actimetrics). FreezeFrame was used to
570 control delivery of the foot shocks and perform freezing analyses. Freezing during fear
571 conditioning was defined as bouts of 1.25 s or longer with minimal changes in pixel luminance.
572
573 *Trace Fear Conditioning*
574 Auditory trace fear conditioning took place on Day 2. After imaging on Day 0, doxycycline was
575 replaced with standard chow and mice were left undisturbed until Day 2. Trace conditioning was
576 performed in Med Associates Chamber with a nine-minute protocol in MedPC. Three auditory
577 stimuli (2.8 kHz, 20 s, pure tone) were presented at 180s, 300s, and 420s. 20 seconds after each
578 tone termination a 2 second, 1.0 mA shock occurred.
579
580 *Imaging during auditory CS presentation*
581 Recording was performed similar as described above, where 27 minutes of spontaneous baseline
582 activity was recorded on Day 0. Two days after trace fear conditioning, the same field of view was
583 recorded again. First, 10 minutes of spontaneous activity was recorded before ten 20-second
584 presentations of the CS+ (2.8kz pure tone) was played, followed by an 80 second ITI. Tone stimuli
585 were delivered via a speaker and Teensy (Arduino) controlled by a BPod (Sanworks) and
586 synchronized with imaging frames. During tone presentations PrairieView recorded TTL pulses
587 sent from BPod to align CS and imaging frames.
588

589 Data Analysis

590 *Image Processing and ROI Extraction*
591 Images were first spatially resized in Fiji (method: averaging, bilinear interpolation) to 256x256
592 (1.58 um/pixel resolution). All image processing was done using custom Python scripts using the
593 CaImAn python package[57] https://github.com/flatironinstitute/CaImAn). Images were first motion

594 corrected using NoRMCorre with non-rigid motion correction implemented in CaImAn. Day 4
595 images were registered to the average template image from Day 0 so cellular ROIs to allow for in
596 alignment across days. Similarly, two-color images (1040 nm time series) were aligned to the
597 920nm functional images as follows. 1040 nm green channel images were motion corrected to
598 the 920 nm GCaMP average image template and these shifts were applied to the 1040 nm red
599 channel images in order to align green/red channels with the ROIs extracted on the 920 nm
600 images. In some cases, the red channel images were motion corrected to the Day 0 average red
601 channel image template and shifts were applied to the green channel. After motion correction,
602 CNMF was used to extract cellular ROIs and dF/F traces. Registration of cell ROIs across days
603 was performed with the CellReg MATLAB GUI.[21] Visual inspection of spatial ROIs and cell
604 registration was performed, and inaccurate spatial ROIs were excluded. For this step, first
605 CellReg output was visualized as a whole with color coded ROIs for registered cells
606 (Supplementary Figure 2A). Next, each ROI pair was plotted on top of the session's mean
607 template image and correlation image (calculated with CaImAn's
608 '*caiman.summary_images.local_correlations*' function) and manually verified as a true registered
609 cell pair (Supplementary Figure 2B). Additionally, ROIs with a SNR less than 4 were discarded
610 based on visual inspection of lower SNR traces. We did this by thresholding ROIs using CaImAns
611 SNR metric for each ROI from '*cnmf.estimates.SNR_comp*'. Cell ROIs were then manually
612 classified as engram or non-engram based on user-picked threshold of mCherry intensity and
613 visual evaluation of their mCherry expression on Day 4, taking into account the soma intensity
614 relative to the local background of each cell (Figure 1D, see mCherry expression analyses below).
615
616 *mCherry expression analyses*
617 We analyzed mCherry expression using motion-corrected, averaged red channel images
618 acquired at 1040 nm following the two-color registration procedure described earlier. A robust
619 increase in overall mCherry fluorescence was observed from Day 0 (D0) to Day 4 (D4)
620 (Supplementary Figure 1B-C), indicating widespread mCherry labeling during the Dox withdrawal
621 period. Notably, this increase was evident across the entire cell population (Supplementary Figure
622 1B).
623 To identify engram cells, we established a threshold for mCherry pixel intensity on D4.
624 These thresholds were manually evaluated to accommodate field-of-view (FOV) signal
625 heterogeneity and to minimize false positives or negatives that could arise from applying a uniform
626 threshold across FOVs with non-uniform luminance. To validate our approach, we quantified
627 mCherry intensity relative to each cell's local background. This was achieved by scaling each
628 cell's ROI coordinates by a factor of 1.5 around its center of mass to generate a larger surrounding
629 ROI. The background region was isolated by subtracting the original ROI from this expanded ROI,
630 and the mean intensity of this surrounding area was calculated. The mean soma intensity was
631 then divided by this background intensity to yield the Relative Intensity metric (Figure 1D). Engram
632 cells displayed higher mCherry fluorescence relative to their local backgrounds (Figure 1D) and
633 also exhibited elevated raw mCherry intensities (Supplementary Figure 1C). We further assessed
634 changes in mCherry expression by calculating the fold change from D0 to D4 (Supplementary
635 Figure 1D). For each cell, this was computed by dividing the D4 mean ROI intensity by the D0
636 intensity.

Finally, to control for potential leaky expression from incomplete doxycycline suppression of TetTag constructs, we excluded cells with high mCherry expression at D0 from the engram classification. Specifically, we removed cells with expression levels exceeding 2.5 standard deviations above the mean ROI intensity at D0. These cells accounted for approximately 2% of the active CA1 population (Supplementary Figure 1A,E).

Calcium deconvolution and event rates

All dF/F traces underwent calcium deconvolution to infer discrete event times. For event detection we utilized an L0 penalty method described in References 59-60.[59,60] Briefly, each cell's dF/F trace is modeled as a noisy readout of underlying calcium fluorescence dynamics. Two parameters are used to fit event times to each cell's trace: gamma and lambda. Gamma is determined by the half-life of the indicator which we set to 0.14 s as reported for the Thy1-GCaMP6f GP.5.17 line.[58] Lambda controls the strictness of the L0 penalty and therefore the sparseness of events, with higher lambda values resulting in higher sparsity. We estimated lambda for each cell similarly to previous reports[61] and adjusted the minimum event size to 5 standard deviations of the noise in the dF/F of each cell. This threshold was chosen based on manual inspection of deconvolved traces with lower SNR and sparser activity.. Mean event rates were calculated using the weighted sum of deconvolved event sizes, in order to account for calcium transients with larger amplitude as follows. For each cell, all detected calcium events had an associated non-zero magnitude, which were summed over the course of each imaging session and divided by total session time. This ensured smaller transients were not treated the same as larger transients when determining calcium event rate. For trace conditioned mice, deconvolved event rates were calculated during each 20s CS trial and then z-scored across cells within mice.

Correlation analyses

Deconvolved traces for cells were binned using bin sizes of 8, 10,16,25,40, 50, 80, 100, and 125 frames. Pairwise Spearman correlations between every pair of cells simultaneously recorded were performed. Only cells active in both Day 0 and Day 4 sessions were used for this analysis. Pairwise correlations were grouped by cell identity and the mean correlation coefficient for all engram/engram, engram/non-engram or non-engram/non-engram was calculated for each animal Figure 4A. When calculating mean correlation during rest and run states (Figure 4B-C), velocity was thresholded as described above, rest and run epochs required a minimum duration of 1s to be included, and sessions were matched for duration in each state. For thresholding correlated pairs, we chose all pairwise correlations exceeding p-value thresholds ranging from 0.01 to 10e-5 and looked at positively correlated pairs. We took the mean of these thresholded correlations within each population, animal and day and calculated the normalized change as D4 / D0.

For Figure 5F-G, we first binarized deconvolved activity traces from either the baseline period or the period of CS-presentations and ITIs. We computed pairwise cross-correlations between cell pairs using a ±60-frame lag window, generating symmetric correlation matrices for both baseline and tone periods. This time window was chosen from rastermap settings that enabled capturing longer sequential patterns. To establish statistical significance, we constructed a null distribution by performing 1000 circular shifted permutations of each cell's activity, preserving autocorrelation while disrupting pairwise timing. The 95th percentile of this null distribution was used as a

threshold to identify significantly correlated pairs, defined as those whose observed cross-correlation exceeded this empirical cutoff.

Rastermap and sequence analysis

To identify sequential dynamics in the deconvolved activity, event traces were binarized and given to rastermap. Rastermap was run using the following parameters {n_clusters=None, nPCs=10, time_lag_window=60, locality=0.1, time_bin=15}, which were similar to recommended parameters for single-cell sorting in hippocampal navigation data. For Figure 3E, cells that participated in rastermap-sorted sequences were chosen from sorted rastermaps, as their sorting algorithm groups sequentially active cells together (Figure 3D). For Figure 3F, velocity correlation was calculated as the Pearson correlation between the summed activity of the population (engram or non-engram) and velocity.

Hierarchical Bayesian GLMs

These HB-GLMs leveraged partial pooling of event rates across animals to increase statistical power. In these HB-GLMs, the slope coefficient β_1 represents the effect of a cell's event rate on the likelihood of tagging, and the intercept β_0 captures baseline tagging variability. Both parameters were estimated for each animal individually under a group-level prior distribution. To avoid prior bias, we used noninformative priors centered β_0 = 0 and β_1 = 0, corresponding to a null hypothesis of no relationship between activity rate and tagging likelihood (Supplementary Figure 4F).

We implemented four variants of a hierarchical Bayesian logistic regression model to analyze the relationship between event rates and population outcomes (i.e., were cells tagged or not during learning) across different animals. Models were fit using the python packages arviz and pymc. Separate models were fit for event rates during 1) rest periods only (Rest model), 2) running bouts only (Run model), 3) both resting and running, with separate regressors for cell's event rates during rest and run (Combined model), and 4) a null model ($\beta_1 = 0$) (Supplementary Figure 4D).

For each animal i and cell j:

Where s is the sigmoid function:

The linear predictor varied by model:

$$\text{Rest model: } p_{ij} = \beta_{0,i} + \beta_{1,i} \times EventRate_{rest\ i,j}$$

$$\text{Running model: } p_{ij} = \beta_{0,i} + \beta_{1,i} \times EventRate_{run\ i,j}$$

$$\text{Combined model: } p_{ij} = \beta_{0,i} + \beta_{1\,rest\,,i} \times EventRate_{rest\ i,j} + \beta_{1run\,,i} \times EventRate_{run\ i,j}$$

$$\text{Null model: } p_{ij} = \beta_{0,i}$$

where the individual-level parameters follow:

$$\beta_{1,i} \sim Normal(\beta_{1_}group, 1)$$

$$\beta_{0,i} \sim Normal(\beta_{0_}group, 1)$$

$$\beta_{1_rest,i} \sim Normal(\beta_{1_rest,i_}group, 1) \text{ [Combined model only]}$$

$$\beta_{1_run,i} \sim Normal(\beta_{1_run,i_}group, 1) \text{ [Combined model only]}$$

And the group-level parameters have the following prior distributions:

$$\beta_{0_}group \sim Normal(0, 10)$$

$$\beta_{1_{rest}}group \sim Normal(0, 10) \text{ [Combined model only]}$$

$$\beta_{1_{run}}group \sim Normal(0, 10) \text{ [Combined model only]}$$

To evaluate model performance, we compared the expected log predictive density using leave-one-out cross-validation (ELPD-LOO). The combined model showed the best predictive performance, with the highest ELPD-LOO value (Supplementary Figure 4G, Combined: -2438). In contrast, both the run-only and null models underperformed relative to the rest-only and combined models, as reflected in their lower LOO values (Supplementary Figure 4G, run: -2445, null: -2456). The Combined model performed significantly better than the Null model (ELPD difference: 17.6 ± 7.2). Notably, the Rest-only model was nearly as informative as the Combined model, with only a small, non-significant ELPD difference, suggesting that rest activity alone captured most of the predictive structure (Supplementary Figure 4G, ELPD-LOO combined: -2438, rest: -2443). These results are consistent with our prior linear regression analyses (Figure 2), as models incorporating rest-period activity demonstrated improved predictive performance. For both Combined and Rest models, the estimated $\beta_{1\,rest}$ values for individual animals were consistently positive and greater than the $\beta_{1\,run}$ values in both combined and rest-only models (Supplementary Figure 4E). Finally, group-level posterior distributions reinforced these effects, as the 95% high-density intervals (HDIs) for $\beta_{1\,rest}$ excluded zero for rest and combined models (Supplementary Figure 4D Combined $\beta_{1\,rest}$ [0.63, 2.39], Rest β_1 [0.85, 2.56]), while the $\beta_{1\,run}$ coefficients were less reliable and had weaker explanatory power (Run $\beta_{1\,run}$: [0.06, 1.37] , Combined $\beta_{1\,run}$ [−0.08, 1.23]). Taken together, these comparisons suggest that rest activity alone captures most of the predictive structure, while adding run activity provides limited additional value.

Histology Confocal Imaging and Cell Counts

Coronal brain sections were imaged using a Zeiss LSM 800 epifluorescence/confocal microscope equipped with a 20x/0.8 NA objective using the Zen2.3 software. Images of dorsal CA1 (dCA1) were acquired in DAPI (405nm), RFP (555 nm), and cFos (GFP, 488) channels. For each animal, 3-5 slices were imaged and averaged for analysis.

Confocal images of dCA1 were preprocessed in FIJI (ImageJ). A custom Fiji macro was used to split channels, adjust brightness and contrast, and separate z-stacks. Regions of interest were delineated with the polygon tool to isolate the pyramidal cell layer of dCA1. For each z-stack, the three central slices with the highest signal intensity were selected for quantification. Cell segmentation and counting were performed using a custom-trained Cellpose3 model and resulting cell counts were exported as NumPy files for averaging across slices, animals, and experimental groups.

In cases where DAPI counts could not be obtained directly, values were estimated on the relationship between countable DAPI cells and the measured area of the DAPI-labeled region. The percentage of mcherry-positive cells was calculated as (mCherry/DAPI x100). For each mouse, a single averaged value across all slices was generated and used for subsequent statistical analyses.

Statistical analysis

All statistical analyses were performed in Python using the `pingouin` (v0.5.3) or `statsmodels` (v0.13.5) packages. We assessed normality using the Shapiro-Wilk test to guide the choice of statistical tests. For comparisons across groups and timepoints, we employed either 2-Way Repeated Measures ANOVAs (for balanced, parametric data) or linear mixed effects models (for unbalanced, non-parametric, or repeated-measures designs), with random intercepts for mice or FOVs when applicable. Post hoc comparisons were conducted using paired (across mice or FOVs) or unpaired t-tests for parametric data, and Wilcoxon signed-rank or Mann-Whitney U tests for non-parametric data, with multiple comparisons corrected using Benjamini-Hochberg FDR, alpha=0.05. Data are presented as mean ± SEM unless otherwise indicated. For regression analyses, 95% confidence intervals are reported.

Spiking Network Model of CA3-CA1

Spiking Network Model of CA3-CA1

We model each neuron's spike train as a Poisson process with time dependent rate $r_i(t)$ given by

$$r_i(t) = \phi\left(\sum_j G_{ij} * \frac{dN_j}{dt}(t)\right) + E_i(t)) \quad (1)$$

Here, $N_j(t)$ counts the total number of spikes neuron j has fired up to time t, and its derivative $\frac{dN_j}{dt} = \sum_k \delta(t - t_j{}^k)$ describes the neuron's spike train as a sum of Dirac delta functions. G is a matrix of synaptic interaction filters, and $*$ denotes a convolution, i.e. $(g * f)(t) = \int_{t_0}^{\infty} dt'\, g(t - t')f(t')$. We take $G_{ij}(s) = J_{ij}\,\frac{1}{\tau}\,exp\,(-s/\tau)$ (for $s \geq 0$) where J_{ij} gives the synaptic weight from neuron j onto neuron i. We take ϕ to be threshold-quadratic, i.e. $\phi(x) = max(x, 0)^2$.

Our synaptic weight matrices were constructed to reflect recurrent E-E connectivity in CA3, as well as recurrent E-I connectivity in both CA1 and CA3 and feedforward connectivity from CA3 to CA1 (Figure 5A). We base our weight matrix J on the connectivity of regions CA1 and CA3 of the hippocampus. We further subdivide both CA1 and CA3 into excitatory engram neurons (E), excitatory non-engram neurons (N), and inhibitory neurons (I). The regional connectivity is given by a 6x6 matrix $\bar{J}$.

Our synaptic weight matrices were constructed to reflect recurrent E-E connectivity in CA3, as well as recurrent E-I connectivity in both CA1 and CA3 and feedforward connectivity from CA3 to CA1 (Figure 5A). We base our weight matrix J on the connectivity of regions CA1 and CA3 of the hippocampus. We further subdivide both CA1 and CA3 into excitatory engram neurons (E), excitatory non-engram neurons (N), and inhibitory neurons (I). The regional connectivity is given by a 6x6 matrix $\underline{J}$.

$$\bar{J} = J_0 \begin{array}{c} \begin{array}{cccccc} CA3E & CA3N & CA3I & CA1E & CA1N & CA1I \end{array} \\ \begin{pmatrix} h & 1 & -h_{I3}g & 0 & 0 & 0 \\ 1 & 1 & -g & 0 & 0 & 0 \\ 1 & 1 & -g_{II} & 0 & 0 & 0 \\ h & 1 & 0 & 0 & 0 & -h_{I1}g \\ 1 & 1 & 0 & 0 & 0 & -g \\ 1 & 1 & 0 & 1 & 1 & -g_{II} \end{pmatrix} \end{array} \begin{array}{c} CA3E \\ CA3N \\ CA3I \\ CA1E \\ CA1N \\ CA1I \end{array}$$

Here, the parameter h describes the strength of engram to engram synapses (in CA3 and CA3 to CA1), relative to the baseline strength of excitatory to excitatory synapses, the parameter g describes the relative strength of inhibitory to excitatory connections, the parameter g_{II} describes the relative strength of inhibitory to inhibitory synapses, and the parameters h_{I3} and h_{I1} describe the strength of the homeostatic inhibitory plasticity, i.e. the increased inhibition recruited by engram cells, in CA3 and CA1, respectively.

Neuron to neuron connectivity is described by a block-wise Erdős-Rényi adjacency matrix A, with sparse excitatory connectivity and dense inhibitory connectivity given by $p_{EE} = 0.1, p_{IE} = 0.8, p_{II} = 0.8, p_{EI} = 0.8$. The connection probabilities do not differ between engram and non-engram cells. Finally, the neuron-to-to neuron weights J_{ij} are given by $J_{ij} = \frac{A_{ij}}{N_{\alpha(j)} p_{\alpha(i)\alpha(j)}} \bar{J}_{\alpha(i)\,\alpha(j)}$ where $\alpha(i)$ gives the region containing neuron i.

Estimating population rates and correlations

In addition to using our stochastic spiking model to simulate neural activity, we calculate estimates for the expected firing rate r_i of each neuron as well as the expected correlation C_{ij} between each pair of neurons. For more details, see [23,62,63]. To find a self-consistent equilibrium rate r_i for each neuron, we substitute r_j for $\frac{dN_j}{dt}$ in Equation 1 and replace convolution with G_{ij} with multiplication by J_{ij} because the expected rate r_j is constant. We then find r by numerically solving

$$r = \phi(J\,r + E).$$

In addition to finding the individual expected rate for each neuron for a fixed neuron-level connectivity matrix J, we can find the expected rate of a neuron in each population, where the expectation is taken both over the random connectivity matrix J and the stochastic spiking. Letting $\underline{r}$ denote the vector of expected rates for each population and $\underline{E}$ denote the mean input to each population, we have

$$\bar{r} = \phi(\bar{J}\bar{r} + \bar{E})$$

We again solve this numerically to find $\underline{r}$. Note that these estimates are all for the mean-field rate, i.e. they do not include corrections to the firing rate resulting from correlations in the input interacting with the nonlinear function ϕ. To account for this, we add a one-loop correction term.[64]

To estimate the expected spike train covariance matrix Σ, we linearize around the expected rate and apply the formula

$$\Sigma = \Delta\, R\, \Delta^T$$

where $\Delta = (I - \phi'(r)\,J)^{-1}$, R is a diagonal matrix with $R_{ii} = r_i$, and $\phi'(r)$ is a diagonal matrix with $\phi'(r)_{ii} = \phi'(r_i)$. We then compute the correlation matrix C from the covariance matrix Σ by $C_{ij} = \frac{\Sigma_{ij}}{\sqrt{\Sigma_{ii}\,\Sigma_{jj}}}$.

As with the rate, we also estimate the expected value for the population-level correlation, i.e. the matrix $\underline{C}$ with entries $\underline{C_{\alpha\beta}}$ giving the expected correlation between a neuron in population α and a neuron in population β where the expectation is taken over both the random connectivity matrix J and the stochastic spiking. Letting $\underline{\Sigma_{\alpha\beta}}$ denote our estimate of the expected covariance between a neuron in population α and a (distinct) neuron in population β, we have

$$\bar{\Sigma} = \bar{\Delta}\,N^{-1}\,\bar{R}\,\bar{\Delta}^T - N^{-1}\,\bar{R}.$$

Here, we define $\bar{\Delta} = (I - \phi'(\bar{r})\,\bar{J})^{-1}$ and use N to denote the diagonal matrix with $N_{\alpha\alpha}$ giving the number of neurons in population α.

For each population, we can also compute the expected variance of a neuron, which is given by

$\overline{\sigma_\alpha} = \overline{\Sigma_{\alpha\alpha}} + \bar{r}_\alpha$Finally, we compute the population correlation matrix $\bar{C}$ by $\overline{C_{\alpha\beta}} = \frac{\overline{\Sigma_{\alpha\beta}}}{\overline{\sigma_\alpha}\,\overline{\sigma_\beta}}$.

References

1. Josselyn, S.A., Köhler, S., and Frankland, P.W. (2015). Finding the engram. Nat Rev Neurosci *16*, 521–534. https://doi.org/10.1038/nrn4000.
2. Josselyn, S.A., and Tonegawa, S. (2020). Memory engrams: Recalling the past and imagining the future. Science *367*. https://doi.org/10.1126/science.aaw4325.
3. Eichenbaum, H. (2017). On the Integration of Space, Time, and Memory. Neuron *95*, 1007–1018. https://doi.org/10.1016/j.neuron.2017.06.036.
4. Denny, C.A., Kheirbek, M.A., Alba, E.L., Tanaka, K.F., Brachman, R.A., Laughman, K.B., Tomm, N.K., Turi, G.F., Losonczy, A., and Hen, R. (2014). Hippocampal memory traces are differentially modulated by experience, time, and adult neurogenesis. Neuron *83*, 189–201. https://doi.org/10.1016/j.neuron.2014.05.018.
5. Liu, X., Ramirez, S., Pang, P.T., Puryear, C.B., Govindarajan, A., Deisseroth, K., and Tonegawa, S. (2012). Optogenetic stimulation of a hippocampal engram activates fear memory recall. Nature *484*, 381–385. https://doi.org/10.1038/nature11028.
6. Ramirez, S., Liu, X., Lin, P.-A., Suh, J., Pignatelli, M., Redondo, R.L., Ryan, T.J., and Tonegawa, S. (2013). Creating a False Memory in the Hippocampus. Science *341*, 387–391. https://doi.org/10.1126/science.1239073.
7. Shpokayte, M., McKissick, O., Guan, X., Yuan, B., Rahsepar, B., Fernandez, F.R., Ruesch, E., Grella, S.L., White, J.A., Liu, X.S., et al. (2022). Hippocampal cells segregate positive and negative engrams. Commun Biol *5*, 1009. https://doi.org/10.1038/s42003-022-03906-8.

8. Chen, B.K., Murawski, N.J., Cincotta, C., McKissick, O., Finkelstein, A., Hamidi, A.B., Merfeld, E., Doucette, E., Grella, S.L., Shpokayte, M., et al. (2019). Artificially Enhancing and Suppressing Hippocampus-Mediated Memories. Current Biology, 1–10. https://doi.org/10.1016/j.cub.2019.04.065.
9. Grella, S.L., Fortin, A.H., Ruesch, E., Bladon, J.H., Reynolds, L.F., Gross, A., Shpokayte, M., Cincotta, C., Zaki, Y., and Ramirez, S. (2022). Reactivating hippocampal-mediated memories during reconsolidation to disrupt fear. Nat Commun *13*, 4733. https://doi.org/10.1038/s41467-022-32246-8.
10. Zhou, Y., Zhu, H., Liu, Z., Chen, X., Su, X., Ma, C., Tian, Z., Huang, B., Yan, E., Liu, X., et al. (2019). A ventral CA1 to nucleus accumbens core engram circuit mediates conditioned place preference for cocaine. Nat Neurosci *22*, 1986–1999. https://doi.org/10.1038/s41593-019-0524-y.
11. Tanaka, K.Z., He, H., Tomar, A., Niisato, K., Huang, A.J.Y., and McHugh, T.J. (2018). The hippocampal engram maps experience but not place. Science *361*, 392–397. https://doi.org/10.1126/science.aat5397.
12. Pettit, N.L., Yap, E.-L., Greenberg, M.E., and Harvey, C.D. (2022). Fos ensembles encode and shape stable spatial maps in the hippocampus. Nature. https://doi.org/10.1038/s41586-022-05113-1.
13. Chen, L., Cummings, K.A., Mau, W., Zaki, Y., Dong, Z., Rabinowitz, S., Clem, R.L., Shuman, T., and Cai, D.J. (2020). The role of intrinsic excitability in the evolution of memory: Significance in memory allocation, consolidation, and updating. Neurobiology of Learning and Memory *173*, 107266. https://doi.org/10.1016/j.nlm.2020.107266.
14. Josselyn, S.A., and Frankland, P.W. (2018). Memory Allocation: Mechanisms and Function. Annual Review of Neuroscience *41*, 389–413. https://doi.org/10.1146/annurev-neuro-080317-061956.
15. Rashid, A.J., Yan, C., Mercaldo, V., Hsiang, H.L., Park, S., Cole, C.J., De Cristofaro, A., Yu, J., Ramakrishnan, C., Lee, S.Y., et al. (2016). Competition between engrams influences fear memory formation and recall. Science *353*. https://doi.org/10.1126/science.aaf0594.
16. Yiu, A.P., Mercaldo, V., Yan, C., Richards, B., Rashid, A.J., Hsiang, H.-L.L., Pressey, J., Mahadevan, V., Tran, M.M., Kushner, S.A., et al. (2014). Neurons Are Recruited to a Memory Trace Based on Relative Neuronal Excitability Immediately before Training. Neuron *83*, 722–735. https://doi.org/10.1016/j.neuron.2014.07.017.
17. Han, J.H., Kushner, S.A., Yiu, A.P., Cole, C.J., Matynia, A., Brown, R.A., Neve, R.L., Guzowski, J.F., Silva, A.J., and Josselyn, S.A. (2007). Neuronal competition and selection during memory formation. Science *316*, 457–460. https://doi.org/10.1126/science.1139438.
18. Tanaka, K.Z., Pevzner, A., Hamidi, A.B., Nakazawa, Y., Graham, J., and Wiltgen, B.J. (2014). Cortical Representations Are Reinstated by the Hippocampus during Memory Retrieval. Neuron *84*, 347–354. https://doi.org/10.1016/j.neuron.2014.09.037.
19. Ryan, T.J., Roy, D.S., Pignatelli, M., Arons, A., and Tonegawa, S. (2015). Engram cells retain memory under retrograde amnesia. Science *348*, 1007–1013. https://doi.org/10.1126/science.aaa5542.
20. Ghandour, K., Ohkawa, N., Fung, C.C.A., Asai, H., Saitoh, Y., Takekawa, T., Okubo-Suzuki, R., Soya, S., Nishizono, H., Matsuo, M., et al. (2019). Orchestrated ensemble activities

constitute a hippocampal memory engram. Nat Commun *10*, 2637. https://doi.org/10.1038/s41467-019-10683-2.

21. Castello-Waldow, T.P., Weston, G., Ulivi, A.F., Chenani, A., Loewenstein, Y., Chen, A., and Attardo, A. (2020). Hippocampal neurons with stable excitatory connectivity become part of neuronal representations. PLoS Biol *18*, e3000928. https://doi.org/10.1371/journal.pbio.3000928.
22. Choi, J.H., Sim, S.E., Kim, J. il, Choi, D.I.I., Oh, J., Ye, S., Lee, J., Kim, T.H., Ko, H.G., Lim, C.S., et al. (2018). Interregional synaptic maps among engram cells underlie memory formation. Science *360*, 430–435. https://doi.org/10.1126/science.aas9204.
23. Uytiepo, M., Zhu, Y., Bushong, E., Chou, K., Polli, F.S., Zhao, E., Kim, K.-Y., Luu, D., Chang, L., Yang, D., et al. (2025). Synaptic architecture of a memory engram in the mouse hippocampus. Science *387*, eado8316. https://doi.org/10.1126/science.ado8316.
24. Kim, S.J., Slocum, A.H., and Scott, B.B. (2022). A miniature kinematic coupling device for mouse head fixation. Journal of Neuroscience Methods *372*, 109549. https://doi.org/10.1016/j.jneumeth.2022.109549.
25. Mocle, A.J., Ramsaran, A.I., Jacob, A.D., Rashid, A.J., Luchetti, A., Tran, L.M., Richards, B.A., Frankland, P.W., and Josselyn, S.A. (2024). Excitability mediates allocation of pre-configured ensembles to a hippocampal engram supporting contextual conditioned threat in mice. Neuron, S0896627324000916. https://doi.org/10.1016/j.neuron.2024.02.007.
26. Joo, H.R., and Frank, L.M. (2018). The hippocampal sharp wave–ripple in memory retrieval for immediate use and consolidation. Nat Rev Neurosci *19*, 744–757. https://doi.org/10.1038/s41583-018-0077-1.
27. Carr, M.F., Jadhav, S.P., and Frank, L.M. (2011). Hippocampal replay in the awake state: a potential substrate for memory consolidation and retrieval. Nature neuroscience *14*, 147–153.
28. Buzsáki, G., and Tingley, D. (2018). Space and Time: The Hippocampus as a Sequence Generator. Trends in Cognitive Sciences *22*, 853–869. https://doi.org/10.1016/j.tics.2018.07.006.
29. Stringer, C., Zhong, L., Syeda, A., Du, F., Kesa, M., and Pachitariu, M. (2025). Rastermap: a discovery method for neural population recordings. Nat Neurosci *28*, 201–212. https://doi.org/10.1038/s41593-024-01783-4.
30. Rao-Ruiz, P., Visser, E., Mitrić, M., Smit, A.B., and Van Den Oever, M.C. (2021). A Synaptic Framework for the Persistence of Memory Engrams. Front. Synaptic Neurosci. *13*, 661476. https://doi.org/10.3389/fnsyn.2021.661476.
31. Zhou, Y., Won, J., Karlsson, M.G., Zhou, M., Rogerson, T., Balaji, J., Neve, R., Poirazi, P., and Silva, A.J. (2009). CREB regulates excitability and the allocation of memory to subsets of neurons in the amygdala. Nat Neurosci *12*, 1438–1443. https://doi.org/10.1038/nn.2405.
32. Park, S., Kramer, E.E., Mercaldo, V., Rashid, A.J., Insel, N., Frankland, P.W., and Josselyn, S.A. (2016). Neuronal Allocation to a Hippocampal Engram. Neuropsychopharmacology *41*, 2987–2993. https://doi.org/10.1038/npp.2016.73.
33. Cai, D.J., Aharoni, D., Shuman, T., Shobe, J., Biane, J., Song, W., Wei, B., Veshkini, M., La-Vu, M., Lou, J., et al. (2016). A shared neural ensemble links distinct contextual memories encoded close in time. Nature *534*, 115–118. https://doi.org/10.1038/nature17955.
34. Zaki, Y., Pennington, Z.T., Morales-Rodriguez, D., Bacon, M.E., Ko, B., Francisco, T.R., LaBanca, A.R., Sompolpong, P., Dong, Z., Lamsifer, S., et al. (2025). Offline ensemble co-

reactivation links memories across days. Nature *637*, 145–155. https://doi.org/10.1038/s41586-024-08168-4.

35. Chen, L., Francisco, T.R., Baggetta, A.M., Zaki, Y., Ramirez, S., Clem, R.L., Shuman, T., and Cai, D.J. (2023). Ensemble-specific deficit in neuronal intrinsic excitability in aged mice. Neurobiology of Aging *123*, 92–97. https://doi.org/10.1016/j.neurobiolaging.2022.12.007.
36. Crestani, A.P., Krueger, J.N., Barragan, E.V., Nakazawa, Y., Nemes, S.E., Quillfeldt, J.A., Gray, J.A., and Wiltgen, B.J. (2019). Metaplasticity contributes to memory formation in the hippocampus. Neuropsychopharmacology *44*, 408–414. https://doi.org/10.1038/s41386-018-0096-7.
37. Delamare, G., Tomé, D.F., and Clopath, C. (2024). Intrinsic neural excitability biases allocation and overlap of memory engrams. J. Neurosci., e0846232024. https://doi.org/10.1523/JNEUROSCI.0846-23.2024.
38. Yang, W., Sun, C., Huszár, R., Hainmueller, T., Kiselev, K., and Buzsáki, G. (2024). Selection of experience for memory by hippocampal sharp wave ripples.
39. Pastalkova, E., Itskov, V., Amarasingham, A., and Buzsáki, G. (2008). Internally Generated Cell Assembly Sequences in the Rat Hippocampus. Science *321*, 1322–1327. https://doi.org/10.1126/science.1159775.
40. Dragoi, G., and Tonegawa, S. (2011). Preplay of future place cell sequences by hippocampal cellular assemblies. Nature *469*, 397–401. https://doi.org/10.1038/nature09633.
41. Dragoi, G. (2024). The generative grammar of the brain: a critique of internally generated representations. Nat. Rev. Neurosci. *25*, 60–75. https://doi.org/10.1038/s41583-023-00763-0.
42. Javed, M.H., Robles-Hernandez, E.M., Patel, R., Haberl, M.G., and Da Silva, S.V. (2024). cfos principal cells and interneurons are strongly reactivated by sharp wave ripples. Preprint, https://doi.org/10.1101/2024.12.17.628897 https://doi.org/10.1101/2024.12.17.628897.
43. Roy, D.S., Park, Y.-G., Kim, M.E., Zhang, Y., Ogawa, S.K., DiNapoli, N., Gu, X., Cho, J.H., Choi, H., Kamentsky, L., et al. (2022). Brain-wide mapping reveals that engrams for a single memory are distributed across multiple brain regions. Nat Commun *13*, 1799. https://doi.org/10.1038/s41467-022-29384-4.
44. Vetere, G., Kenney, J.W., Tran, L.M., Xia, F., Steadman, P.E., Parkinson, J., Josselyn, S.A., and Frankland, P.W. (2017). Chemogenetic interrogation of a brain-wide fear memory network in mice. Neuron *94*, 363–374.
45. Villette, V., Malvache, A., Tressard, T., Dupuy, N., and Cossart, R. (2015). Internally Recurring Hippocampal Sequences as a Population Template of Spatiotemporal Information. Neuron *88*, 357–366. https://doi.org/10.1016/j.neuron.2015.09.052.
46. Barron, H.C., Vogels, T.P., Behrens, T.E., and Ramaswami, M. (2017). Inhibitory engrams in perception and memory. Proc. Natl. Acad. Sci. U.S.A. *114*, 6666–6674. https://doi.org/10.1073/pnas.1701812114.
47. Sadeh, S., and Clopath, C. (2021). Inhibitory stabilization and cortical computation. Nat Rev Neurosci *22*, 21–37. https://doi.org/10.1038/s41583-020-00390-z.
48. Morrison, D.J., Rashid, A.J., Yiu, A.P., Yan, C., Frankland, P.W., and Josselyn, S.A. (2016). Parvalbumin interneurons constrain the size of the lateral amygdala engram. Neurobiology of Learning and Memory *135*, 91–99. https://doi.org/10.1016/j.nlm.2016.07.007.

1006 49. Yap, E.-L., Pettit, N.L., Davis, C.P., Nagy, M.A., Harmin, D.A., Golden, E., Dagliyan, O., Lin,
1007 C., Rudolph, S., Sharma, N., et al. (2021). Bidirectional perisomatic inhibitory plasticity of a
1008 Fos neuronal network. Nature *590*, 115–121. https://doi.org/10.1038/s41586-020-3031-0.
1009 50. Rajasethupathy, P., Sankaran, S., Marshel, J.H., Kim, C.K., Ferenczi, E., Lee, S.Y., Berndt,
1010 A., Ramakrishnan, C., Jaffe, A., Lo, M., et al. (2015). Projections from neocortex mediate top-
1011 down control of memory retrieval. Nature *526*, 653–659. https://doi.org/10.1038/nature15389.
1012 51. Tayler, K.K., Tanaka, K.Z., Reijmers, L.G., and Wiltgen, B.J. (2013). Reactivation of Neural
1013 Ensembles during the Retrieval of Recent and Remote Memory. Current Biology *23*, 99–106.
1014 https://doi.org/10.1016/j.cub.2012.11.019.
1015 52. Ahmed, M.S., Priestley, J.B., Castro, A., Stefanini, F., Solis Canales, A.S., Balough, E.M.,
1016 Lavoie, E., Mazzucato, L., Fusi, S., and Losonczy, A. (2020). Hippocampal Network
1017 Reorganization Underlies the Formation of a Temporal Association Memory. Neuron *107*,
1018 283-291.e6. https://doi.org/10.1016/j.neuron.2020.04.013.
1019 53. MacDonald, C.J., Carrow, S., Place, R., and Eichenbaum, H. (2013). Distinct hippocampal
1020 time cell sequences represent odor memories in immobilized rats. J Neurosci *33*, 14607–
1021 14616. https://doi.org/10.1523/JNEUROSCI.1537-13.2013.
1022 54. Taxidis, J., Pnevmatikakis, E.A., Dorian, C.C., Mylavarapu, A.L., Arora, J.S., Samadian, K.D.,
1023 Hoffberg, E.A., and Golshani, P. (2020). Differential Emergence and Stability of Sensory and
1024 Temporal Representations in Context-Specific Hippocampal Sequences. Neuron *108*, 984-
1025 998.e9. https://doi.org/10.1016/j.neuron.2020.08.028.
1026 55. Ma, M., Simoes De Souza, F., Futia, G.L., Anderson, S.R., Riguero, J., Tollin, D., Gentile-
1027 Polese, A., Platt, J.P., Steinke, K., Hiratani, N., et al. (2024). Sequential activity of CA1
1028 hippocampal cells constitutes a temporal memory map for associative learning in mice.
1029 Current Biology *34*, 841-854.e4. https://doi.org/10.1016/j.cub.2024.01.021.
1030 56. Lucchetti, J., Fracasso, C., Balducci, C., Passoni, A., Forloni, G., Salmona, M., and Gobbi, M.
1031 (2019). Plasma and Brain Concentrations of Doxycycline after Single and Repeated Doses in
1032 Wild-Type and APP23 Mice. J Pharmacol Exp Ther *368*, 32–40.
1033 https://doi.org/10.1124/jpet.118.252064.
1034 57. Robertson, A., Perea, J., Tolmachova, T., Thomas, P.K., and Huxley, C. (2002). Effects of
1035 mouse strain, position of integration and tetracycline analogue on the tetracycline conditional
1036 system in transgenic mice. Gene *282*, 65–74. https://doi.org/10.1016/S0378-1119(01)00793-
1037 4.
1038 58. DeNardo, L.A., Liu, C.D., Allen, W.E., Adams, E.L., Friedmann, D., Fu, L., Guenthner, C.J.,
1039 Tessier-Lavigne, M., and Luo, L. (2019). Temporal evolution of cortical ensembles promoting
1040 remote memory retrieval. Nat Neurosci *22*, 460–469. https://doi.org/10.1038/s41593-018-
1041 0318-7.
1042 59. DeNardo, L., and Luo, L. (2017). Genetic strategies to access activated neurons. Current
1043 Opinion in Neurobiology *45*, 121–129. https://doi.org/10.1016/j.conb.2017.05.014.
1044 60. Murthy, B.K.B., Somatakis, S., Ulivi, A.F., Klimmt, H., Castello-Waldow, T.P., Haynes, N.,
1045 Huettl, R.E., Chen, A., and Attardo, A. (2023). Arc-driven mGRASP highlights CA1 to CA3
1046 synaptic engrams. Front. Behav. Neurosci. *16*, 1072571.
1047 https://doi.org/10.3389/fnbeh.2022.1072571.

1048 61. Hyun, J.H., Nagahama, K., Namkung, H., Mignocchi, N., Roh, S.-E., Hannan, P., Krüssel, S.,
1049 Kwak, C., McElroy, A., Liu, B., et al. (2022). Tagging active neurons by soma-targeted Cal-
1050 Light. Nat Commun *13*, 7692. https://doi.org/10.1038/s41467-022-35406-y.
1051 62. Kim, C.K., Sanchez, M.I., Hoerbelt, P., Fenno, L.E., Malenka, R.C., Deisseroth, K., and Ting,
1052 A.Y. (2020). A Molecular Calcium Integrator Reveals a Striatal Cell Type Driving Aversion.
1053 Cell *183*, 2003-2019.e16. https://doi.org/10.1016/j.cell.2020.11.015.
1054 63. Pouget, C., Morier, F., Treiber, N., García, P.F., Mazza, N., Zhang, R., Reeves, I., Winston,
1055 S., Brimble, M.A., Kim, C.K., et al. (2024). Deconstruction of a memory engram reveals distinct
1056 ensembles recruited at learning. Preprint at bioRxiv,
1057 https://doi.org/10.1101/2024.12.11.627894 https://doi.org/10.1101/2024.12.11.627894.
1058 64. Sanchez, M.I., Nguyen, Q.-A., Wang, W., Soltesz, I., and Ting, A.Y. (2020). Transcriptional
1059 readout of neuronal activity via an engineered Ca^{2+} -activated protease. Proc. Natl. Acad. Sci.
1060 U.S.A. *117*, 33186–33196. https://doi.org/10.1073/pnas.2006521117.
1061 65. Jung, J.H., Wang, Y., Rashid, A.J., Zhang, T., Frankland, P.W., and Josselyn, S.A. (2023).
1062 Examining memory linking and generalization using scFLARE2, a temporally precise neuronal
1063 activity tagging system. Cell Reports *42*, 113592.
1064 https://doi.org/10.1016/j.celrep.2023.113592.
1065

FIGURES

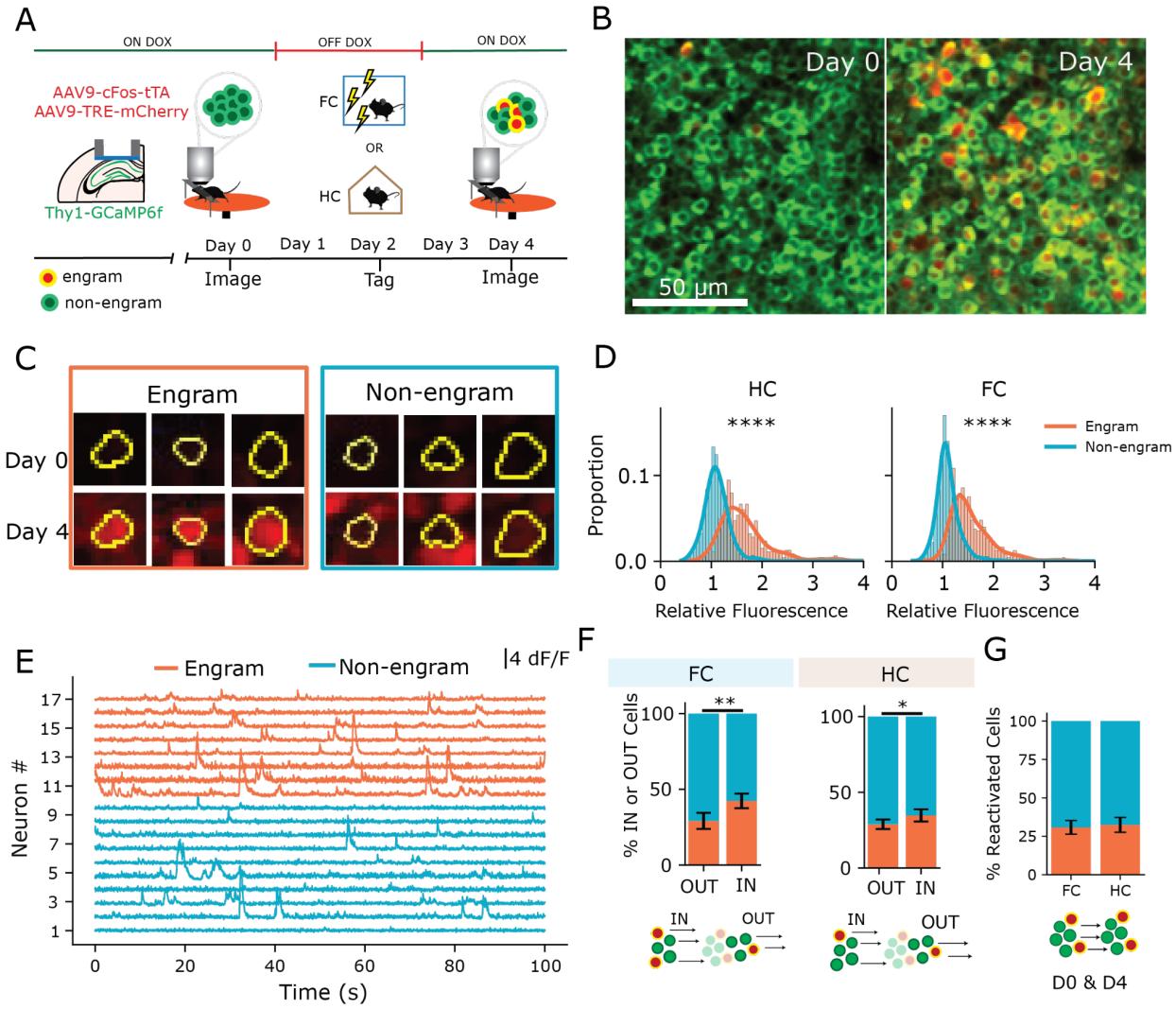

Figure 1. Imaging spontaneous activity in engram cells before and after learning

A) Experimental timeline. Doxycycline (Dox) is removed after imaging on Day 0 to open mCherry tagging window. Mice are off dox Days 1-2 and either fear conditioned on Day 2 or remain in homecage. Dox is replaced on Day 2 and spontaneous imaging of the same CA1 population is repeated on Day 4.

B) Example dual color FOV before and after tagging.

C) Representative engram and non-engram cells before and after mCherry tagging.

D) Relative fluorescence of mCherry expression in engram vs non engram cells on Day 4 (engram vs non-engram cells: HC $p < 0.0001$, FC $p < 0.0001$)

E) Representative calcium traces of spontaneous activity in engram and non-engram cells

F) Percent of cells active on D0 only (OUT cells) and D4 only (IN cells). 2Way RM ANOVA Group x Session, Group: p=0.53, Session p=0.00003, Interaction p=0.03 Left: FC In v Out p = 0.0007 Right HC: p = 0.045.

G) Percent of each cell type stably active on both days. (T-test FC vs HC $T_{8.3}$ = -0.55, p=0.60)

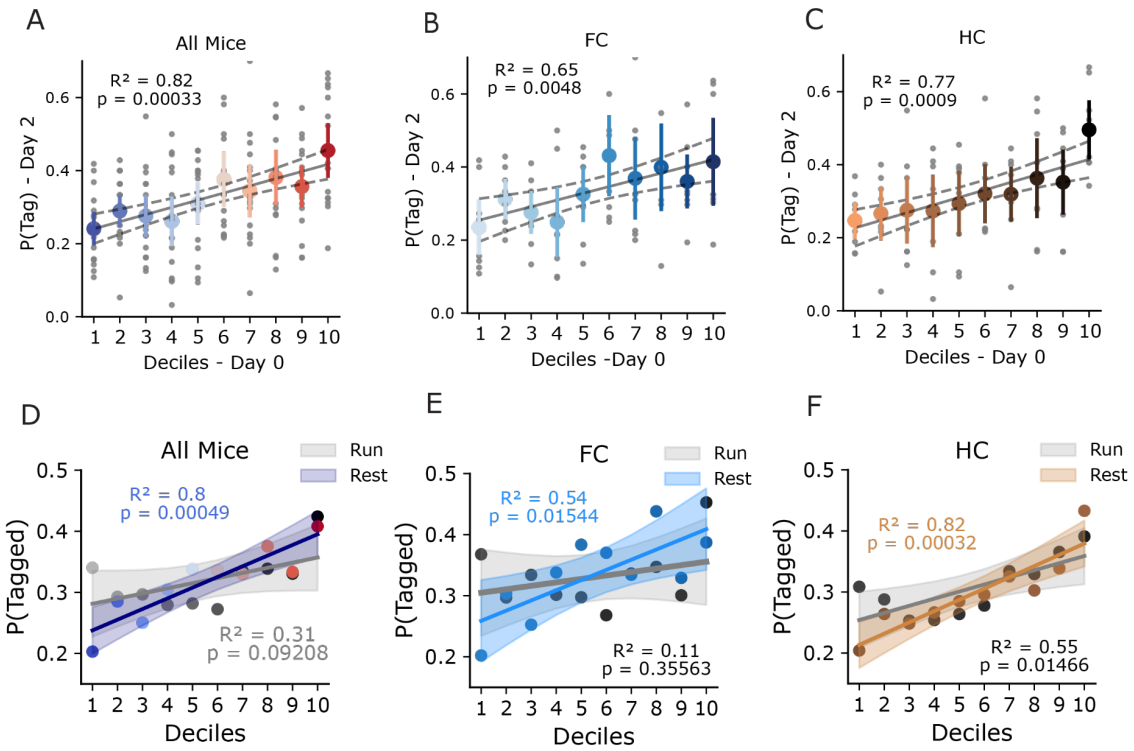

Figure 2. Day 0 spontaneous activity predicts engram allocation two days before tagging

A) Linear regression of baseline calcium activity deciles and probability of Fos-tagging. Blue colors: least active, red: most active. All mice (FC and HC), n=16, R^2 = 0.82, p = 0.00033.

B) FC mice regression of baseline calcium activity deciles and probability of Fos-tagging. light colors: least active, dark colors: most active. n = 8; R^2 = 0.64, p = 0.0048.

C) HC mice regression of baseline calcium activity deciles and probability of Fos-tagging. light colors: least active, dark colors: most active. n = 8; R^2 = 0.77, p = 0.0009.

D) Linear regression of baseline calcium activity split by behavioral state: Rest period activity (navy) or run period activity (gray) . Rest: R^2 = 0.8, p = 0.00049; Run: R^2 = 0.31, p = 0.09

E) Same as D) but for FC mice only. Rest (blue) : R^2 = 0.54, p = 0.015; Run (gray): R^2 = 0.11, p = 0.35

F) Same as D) but for HC mice only. Rest (brown) R^2 = 0.82, p = 0.00032; Run (gray) R^2 = 0.55, p = 0.015

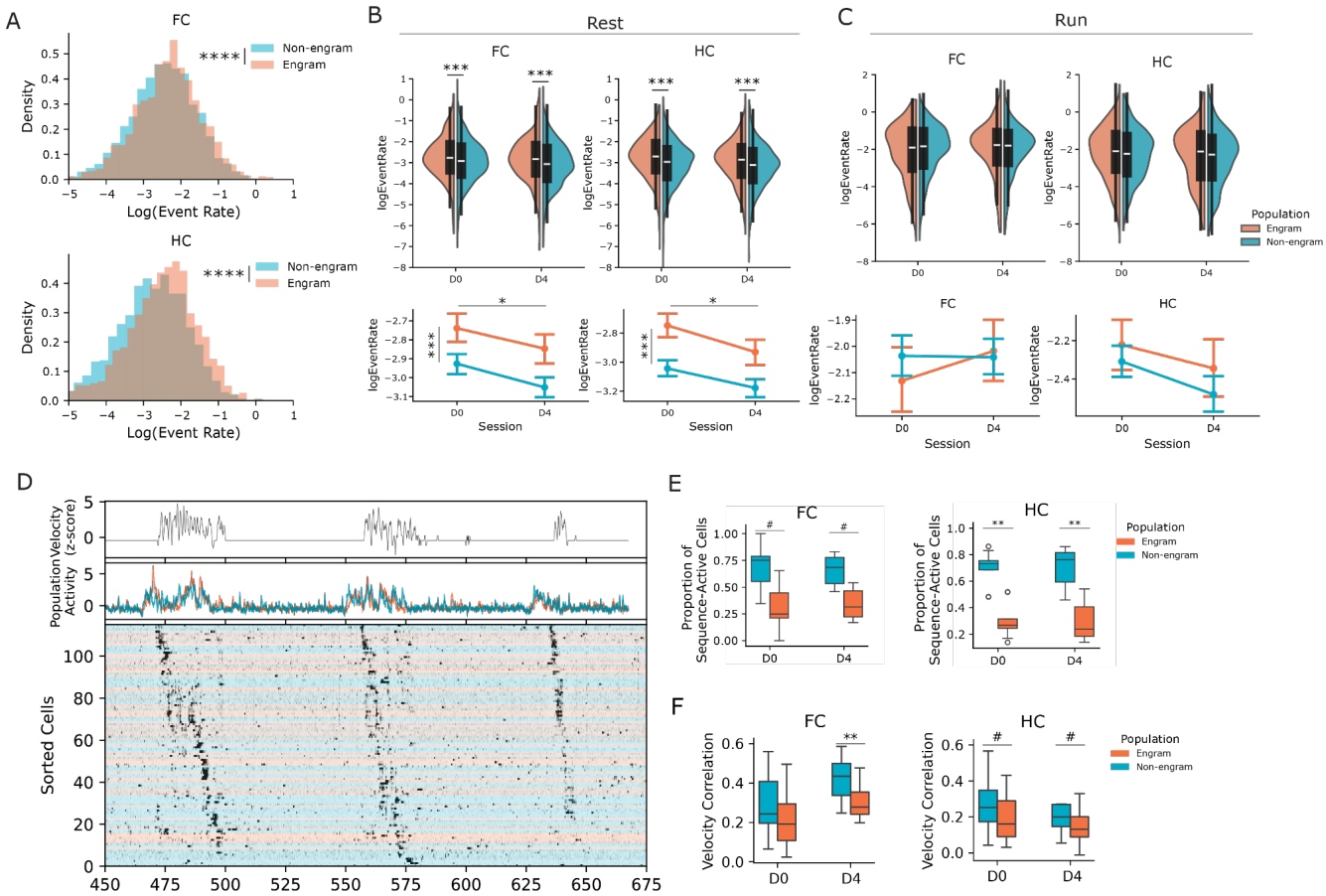

Figure 3. Engram and non-engram populations are differentially modulated by behavior state

A) Distribution of calcium event rates for engram and non-engram cells for each group. Linear mixed effects model, Population x Session. Main effect of Population, *p = 3e-9* Session *p* = 0.18

B) Average calcium event rates during rest periods across sessions for each population. Linear mixed effects model, Effect of Population p=0.004, Session p=0.026, Group p= 0.198. (n=7 FC, n=6 HC)

C) Average calcium event rates during run periods across sessions for each population. Linear mixed effects model, no significant main effects or interactions. Main effect of Population p=0.145, Session p=0.875, Group p=0.430

D) Example rastermap sorting of sequential activity associated with locomotion bouts. Top: normalized velocity. Middle: Summed population activity for engram and non-engram populations. Bottom: sorted rasterplot from rastermap, color-coded by cell type.

E) Example sorted rasterplot demonstrating locomotion related sequential activity. Top: normalized velocity, Middle: summed population activity of engram (orange) and non-engram (teal) cells. Bottom: sorted rasterplot, rows are color coded by cell population (engram or non-engram)

F) Proportion of sequence-participating cells from each population in FC and HC groups. 2Way RM ANOVA, Population x Day. FC Population *p*=0.0096, Interaction *p*=0.38, HC

Population *p*=0.0005, Interaction *p*=0.91. Pairwise t-tests, FC (n=12 FOVs), HC (n=20 FOVs).

G) Velocity correlation of each population. 2Way RM ANOVA Population x Day, FC Population p=0.04, Day p=0.15, Interaction p=0.41, HC Population p=0.05, Day p=0.18, Interaction p=0.96. Pairwise t-tests FC (n=12 FOVs), D0: p=0.3, D4 p=0.005. HC (n=20 FOVs) D0: p=0.08 ,D4 p=0.08.

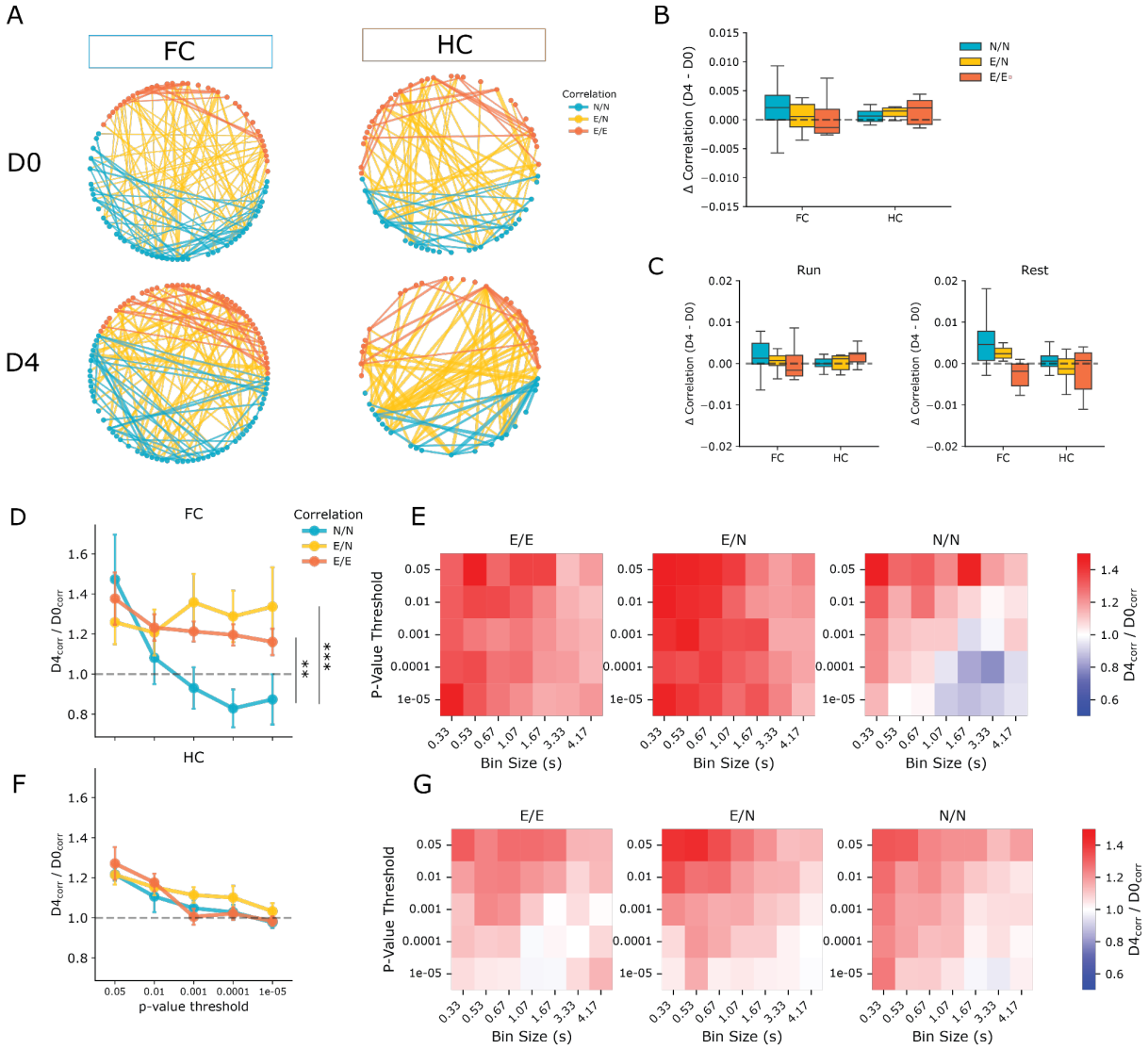

Figure 4. A subset of engram correlations increase during rest after FC

A) Example network graphs displaying Spearman correlations between cells from one FC and one HC mouse. Top: Day 0, Bottom: Day 4. For simplicity, the top 2% of correlations are shown as edges between nodes, scaled by their correlation strength. Orange nodes

indicate engram cells, teal nodes indicate non-engram cells. Orange edges = engram/engram (E/E) correlations, yellow edges = engram/non-engram (E/N) correlations, teal edges = non-engram/non-engram (N/N) correlations. Cell ID sorting is consistent across both days.

B) No change in mean Spearman's correlation across the whole session from D0 to D4 for pairwise correlations between engram/engram cells (orange: E/E), engram/non-engram cells (yellow: E-N), and non-engram/non-engram cells (teal: N/N). Linear mixed effects model, Group x Population. Main effect of Group *(p* = 0.31), Population (*p* = 0.53). A trend-level interaction was found for the FC x E/E effect compared to HC, N/N (*p* = 0.07).

C) No change in mean Spearman's correlation during rest and run states after controlling for time. Left: Rest; Mixed ANOVA Group x Population, Main effect of Group: *p* = 0.17, Population: *p* = 0.18, Interaction: *p* = 0.66. Right: Run; Linear mixed effects model Group x Population. Main effect of Group: *p* = 0.45, Population: E/N *p* = 0.93, E/E *p* = 0.44, FC x E/E *p* = 0.12

D) Normalized change in correlations for thresholded cell pairs across significance levels in FC mice. A bin size of 1.7 seconds was used. Linear mixed effects model, Group x Population interaction. E/E x FC and E/N x FC interactions *p* = 0.002 and *p* = 0.0005 respectively.

E) Heatmap of normalized change in correlation for thresholded pairs across timescales (x-axis, bin sizes) and significance thresholds (y-axis, p-values) in FC mice. Red: increase in correlation across days, Blue: decrease across days, white: no change.

F) Normalized change in correlations for thresholded cell pairs across significance levels in HC mice. A bin size of 1.7 seconds was used.

G) Heatmap of normalized change in correlation for thresholded pairs across timescales (bin sizes) and significance thresholds (p-values) in HC mice. Red: increase in correlation across days, Blue: decrease across days, white: no change.

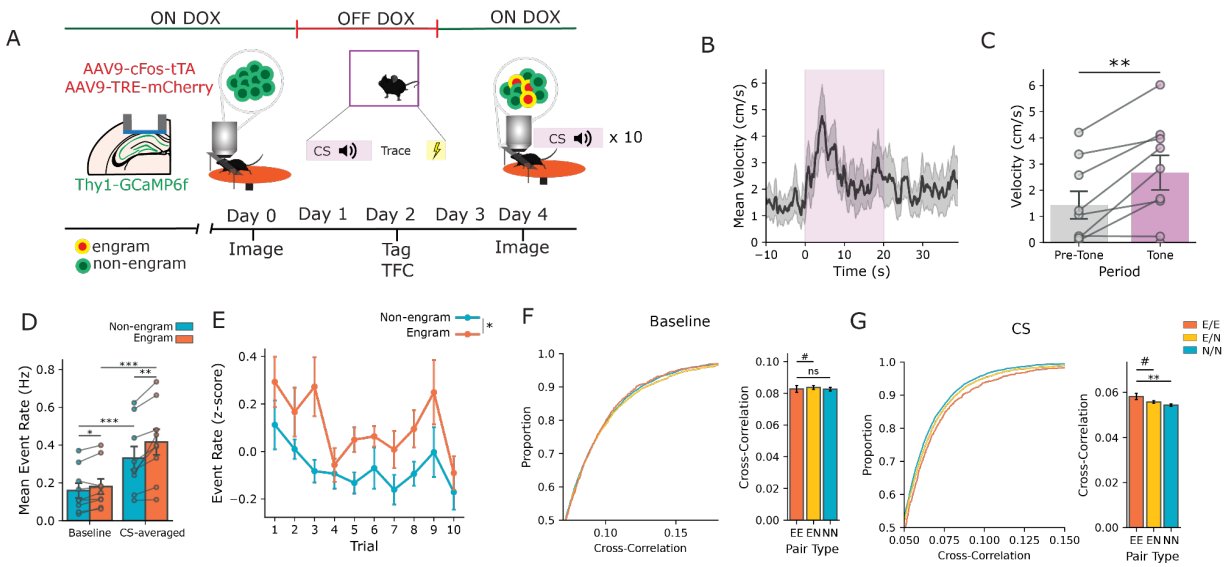

Figure 5. Engram activity during cued reactivation

A) Schematic of experiment timeline for recording engram CS reactivation after trace fear conditioning.

B) Trial averaged velocity trace upon CS presentation during imaging on Day 4, Recall. N = 9.

C) Animal-wise increase in average velocity during CS presentation. Paired t-test p = 0.005, N=9.

D) Increase in event rate among engram cells persists during CS presentations. 2way RM ANOVA Population x Epoch, Population p = 0.002, Epoch p = 0.0001, Population x Epoch p = 0.01. Engram vs Non-engram t-tests: Baseline p = 0.02, CS-averaged p = 0.003. N=9 mice.

E) Event rates across trials in engram and non-engram cells. Linear Mixed Effects Model Population x Trial. Population p = 0.015, Trial p = 0.06, Population x Trial: p = 0.74, N=9 mice

F) Cross correlations of cell pairs during Baseline imaging. Error bars represent 95% CI. Linear Mixed Effects Model Main Effect of Population E/N p = 0.08, N/N p = 0.13, n = 12,532 cell pairs, N=9 mice.

G) Cross correlations of cell pairs during CS presentations and ITIs. Error bars represent 95% CI. Linear Mixed Effects Model Main Effect of Population E/N p = 0.07, N/N p=0.003. n=16,004 cell-pairs, N=9 mice.

SUPPLEMENTARY FIGURES

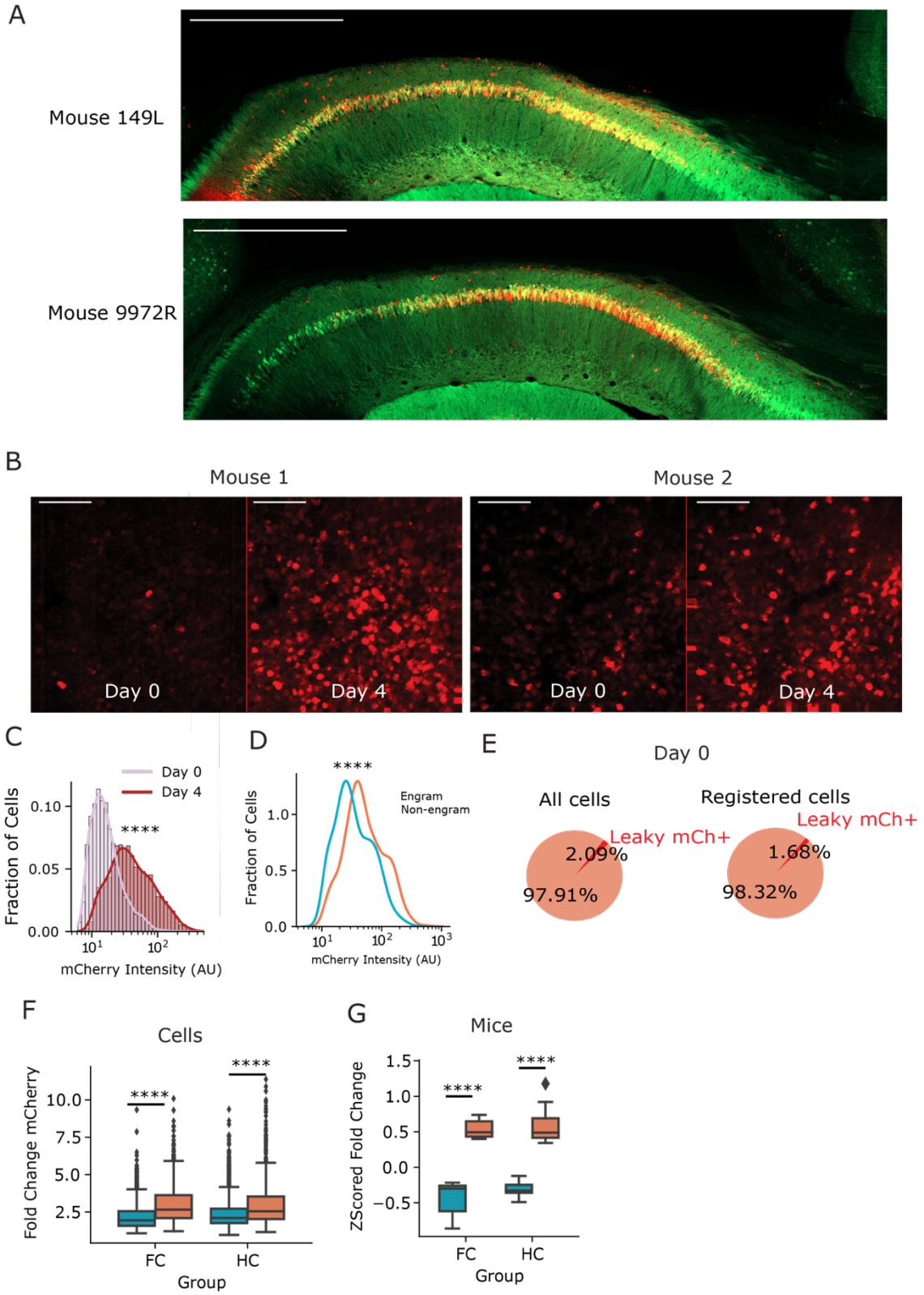

Supplementary Figure 1. Characterization of tetTag with in vivo imaging & fear conditioning behavior

A) Two example histological sections of FC imaging mice. Mice were taken Off dox at the end of the experiment to check viral spread. Scale bar is 200 µm.
B) Two example FOVs for tet-driven mCherry expression across days in vivo. mCherry tagging increases after Day 2 and is measured on Day 4. Scale bars are 100 µm.
C) Increase in mCherry intensity of cells quantified from Day 0 and Day 4. Wilcoxon signed-rank test W=119, p=0.0)
D) On Day 4, tagged engram cells had significantly higher expression of mCherry (Mann-Whitney U Test: U= 952681.0, p=4.1e-36)
E) Percentage of active cells on Day 0 with high, leaky mCherry expression. Approximately 2% of active cells demonstrated high expression on Day 0 before tagging and were not classified as engram cells.
F) Engram cells in both FC and HC mice demonstrated a higher Fold Change in mCherry expression from Day 0 to Day 4 (FC Mann Whitney U Test U= 101666.0, p<0.0001, HC U= 143761.0, p<0.0001)
G) Mean Z-Scored Fold Change in mCherry expression across mice. 2Way RM ANOVA Group X Population (Group F 1.639100, p= 0.2; Population F=161, p=3.9e-13; Interaction F = 0.18, p=0.6

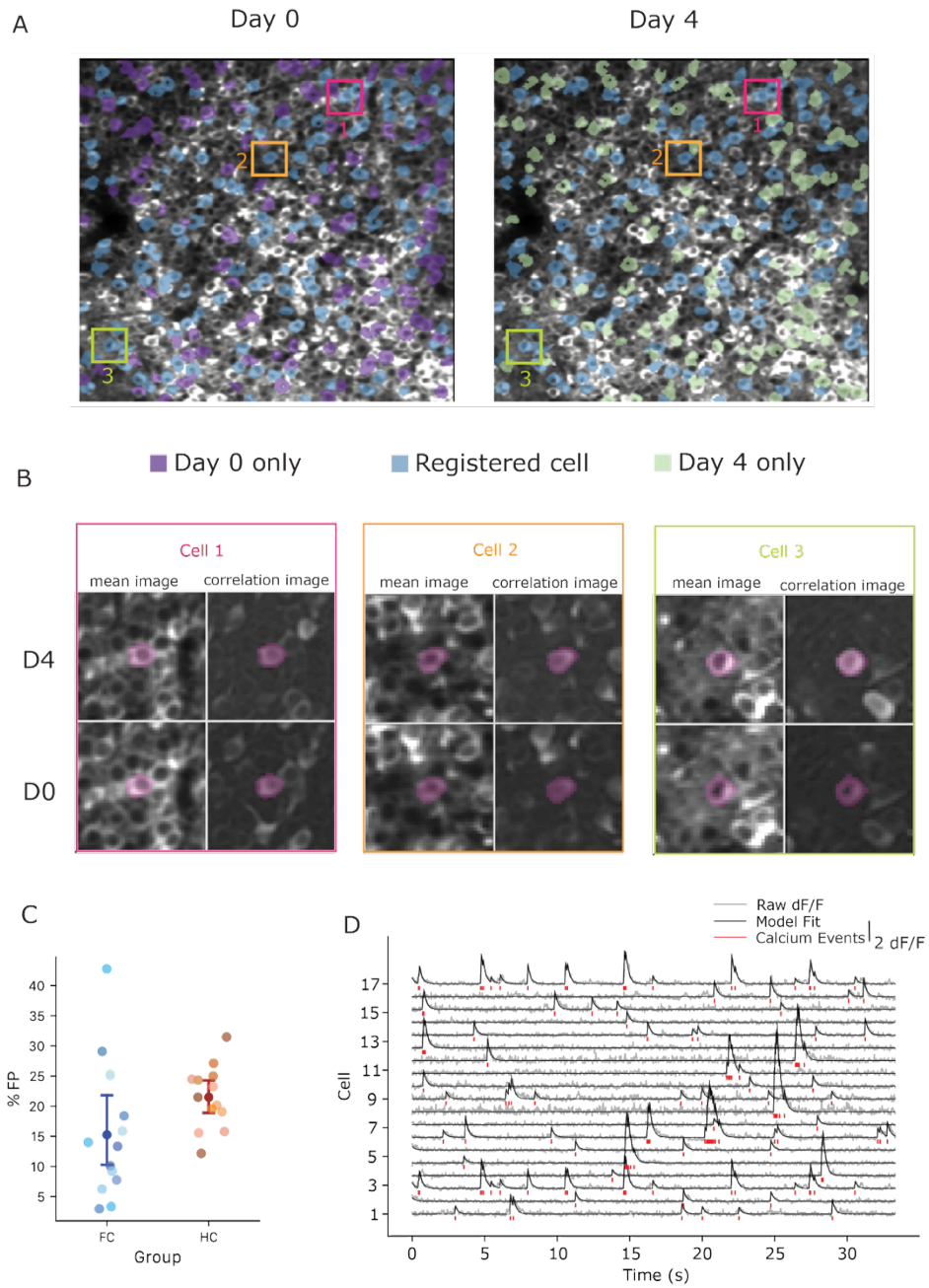

1206

1207 Supplementary Figure 2. Cell registration quantification and
1208 calcium deconvolution.

1209 A) Example FOV of cell registration across 4 days. Blue cells: registered, green cells: D4
1210 only, purple cells: D0 only

1211 B) Example registered cell pairs plotted over mean projection image and correlation image
1212 on each day

C) Proportion of False Positive (FP) registered cell ROIs for each mouse/FOV. Manual evaluation of cells considered false positives if 1 of 3 criteria were met: 1) CNMF spatial footprint did not represent a whole/true cell, 2) if the identified pair from CellReg was not a true match or 3) if CNMF spatial footprint overlapped between 2 cells or 4) the CNMF spatial footprint was in a dark area of the FOV.

D) Example dF/F traces with respective deconvolved events below. Deconvolution model fit (black) overlaid on top of raw dF/F (gray), calcium events shown below each transient (red).

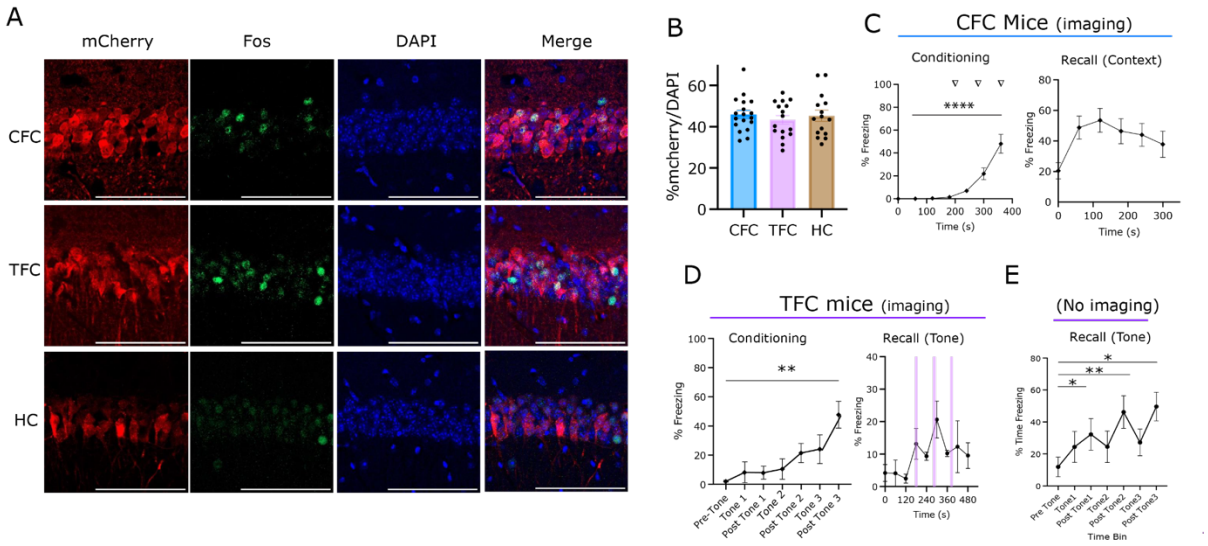

Supplementary Figure 3. Tet-tag histology and fear conditioning behavior.

A) Representative histological sections of tet Tag (cFos-tTA, TRE-mCherry) expression in CA1. 3 groups of mice CFC (n=18), TFC (n=15) or HC (n=16) underwent tagging, with either contextual fear conditioning (CFC) , trace fear conditioning (TFC) or remained in homecage (HC) on Day 2 of a 48 hour off-dox window. 2 days after tagging, mice underwent recall (or remained in homecage) and were sacrificed 90 minutes later for Fos expression.

B) Percentage of mCherry / DAPI (left) tagged cells or Fos (right) in each group. One Way ANOVA, $p = 0.70$.

C) Freezing behavior of CFC mice from 2p experiments. Freezing during CFC (left, One Way ANOVA $p<0.0001$) and Recall (right). Recall took place 2 days after imaging ended (Day 6 relative to first imaging day).

D) Freezing behavior of TFC mice from 2p experiments. Freezing during TFC (left, One Way ANOVA $p=0.0004$ n=8) and Tone recall (right). In a subset of mice (n=3) Recall took place 2 days after imaging ended, in a neutral context (Day 6 relative to first imaging day).

E) Additional cohort of TFC mice that demonstrate freezing to tone CS in a neutral context. One Way ANOVA, pairwise t-tests. * $p<0.05$, ** $p<0.01$.

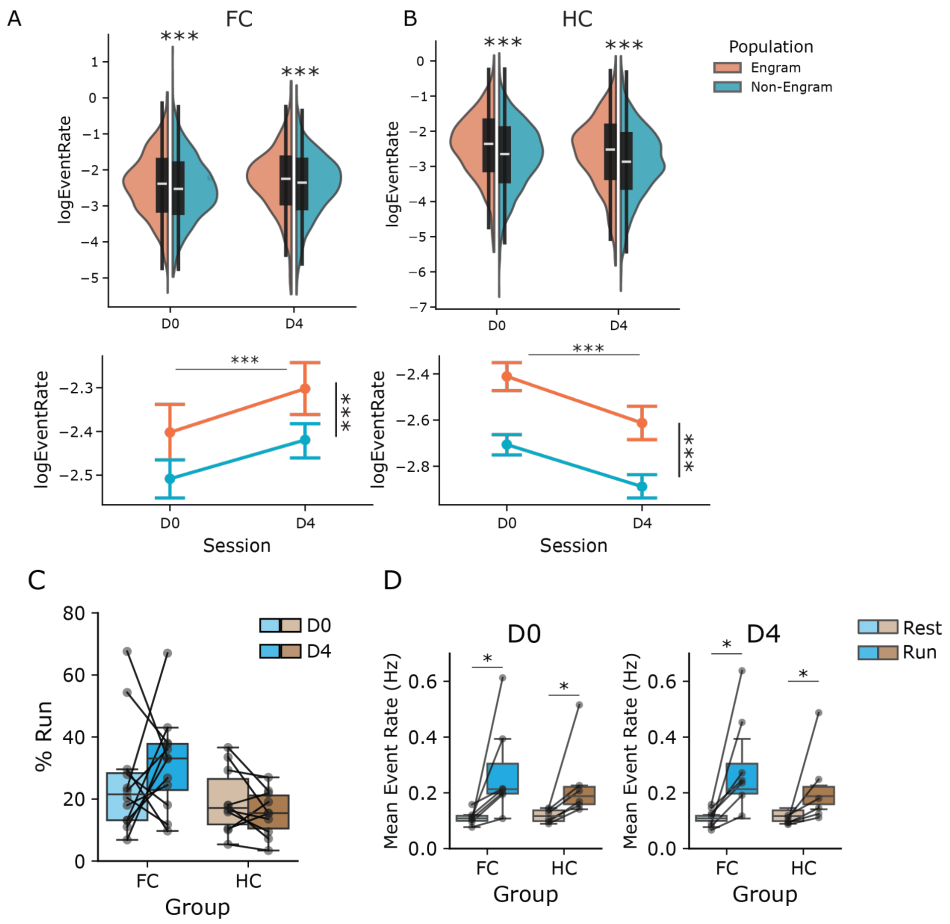

Supplementary Figure 4. Supplemental Rate Analyses

A. Average calcium event rates across sessions for FC mice (n=8) . Linear mixed effects model Group x Population x Session, Main Effect of Population *p = 0.003,* Session *p*=0.143*,* Group *p*=0.354 Group x Session p=0.001.
B. Average calcium event rates during rest periods across sessions for HC mice (n=8) . Linear mixed effects model, Group x Population x Session, Main Effect of Population *p = 0.003,* Session *p*=0.143*,* Group *p*=0.354 Group x Session p=0.001.
C. % Time running for FC (blue) and HC (brown) groups. Mixed Effects Model, Group x Session, Group: *p* = 0.3264, Session: *p* = 0.2710, Interaction: *p* = 0.2207. Points represent FOVs from FC (n=12 FOVs) or HC (n=10 FOVs) across mice.
D. Mean event rates during rest and run periods on each Day. Run periods had significantly higher event rates.

   Left D0: Group p = 0.9188, State, p = 0.0039, Interaction, p = 0.5758 Pairwise tests (Rest vs Run) FC: p=0.03125, HC p=0.0.03125.

   Right D4: Group, p = 0.8557, p = 0.0006, Interaction : p = 0.3458. Pairwise tests (Rest vs Run) FC: p=0.03125, HC p=0.03125. Points represent animals from FC (n=7) or HC (n=6).

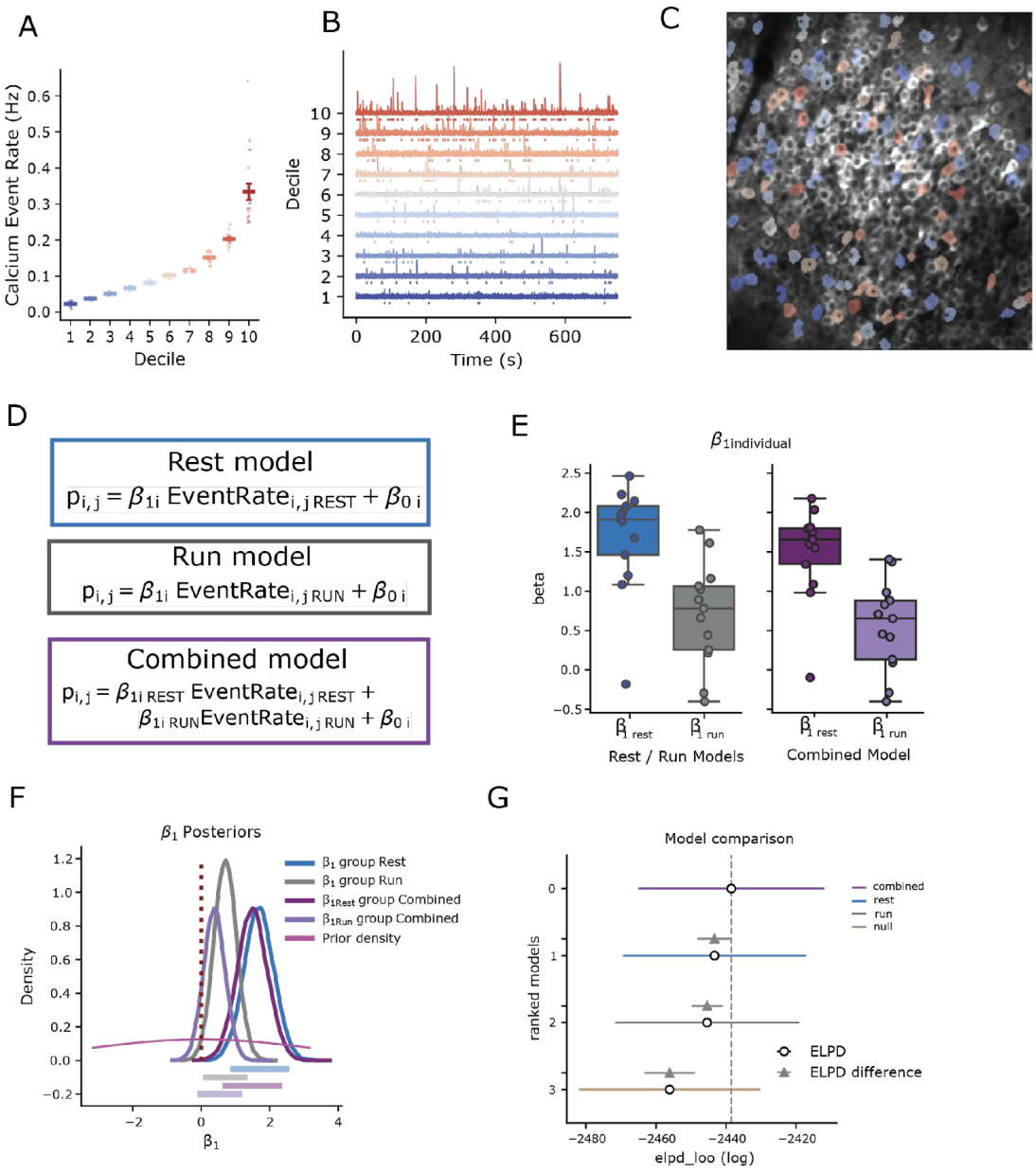

Supplementary Figure 5. Model-based analysis of engram cell firing

A) Example animal with cells split into deciles. Warm = higher activity, cool = less active.
B) Example dF/F traces and calcium events from example cell in each decile
C) Distribution of cells in each decile throughout the example FOV.
D) Setup for different variants of hierarchical GLM. Null model not shown, but equivalent to $\beta_1 = 0$ (intercept only). For mouse i, and cell j, probability of Fos-tagging is modeled as a function calcium event rate governed by animal level parameter β_1, and β_0 represents a bias term in baseline tagging variability across mice.

E) Individual β_1 values for each animal across rest, run and combined models. β_1 in the rest only model (blue) and β_1^{rest} in the combined model (dark purple) both have greater magnitudes across all individual animals.

F) Posterior distributions for group level $\beta_{1\ group}$ coefficients compared to prior distribution (pink). Horizontal lines indicate 95% high-density interval for each model group level posterior. β_1 for rest model (blue) β_1^{rest} (dark purple) both span intervals further from 0 indicating event rate during rest is more informative for predicting likelihood of tagging.

G) Model comparison with ELPD-LOO (Expected Log Predictive Density from Leave-One-Out Cross-Validation) metrics for each model. Higher value indicates better predictive power. Standard error of difference between models shown in gray triangle intervals. The combined model performs the best, while run and null models perform significantly worse. The rest only model performs close to the combined model.

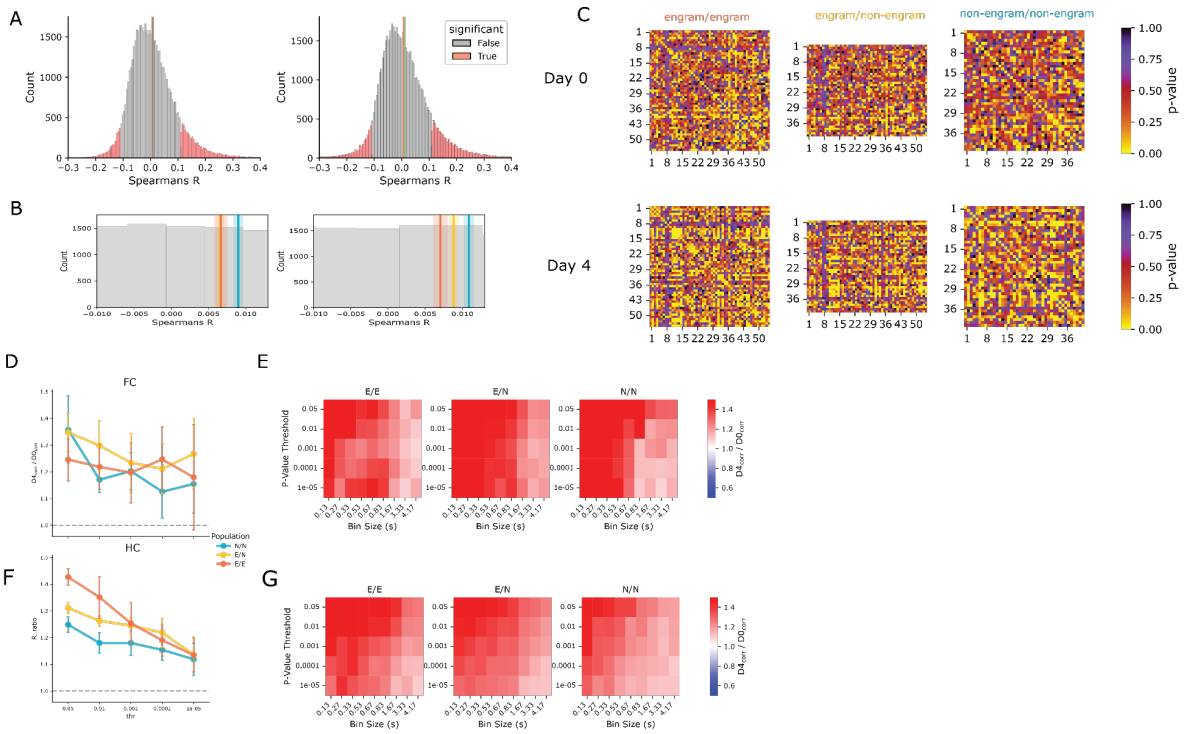

Supplementary Figure 6. Additional correlation analyses

A) Histograms of all Spearman coefficient values with below insets of mean values across mice.
B) Inset of mean Spearmans R coefficient overlaid over distributions from A)
C) P-values for correlation matrix shown in Figure 4A. A subset of cells have significantly correlated cells. Correlations for Figures 4D-G were thresholded based on p-value significance (p<0.05 to p<10e-5).
D) Normalized change in correlations for thresholded cell pairs across significance levels. A bin size of 1.7 seconds was used. LME Group X Population interaction. E/E X FC and E/N x FC interactions p = 0.65 and p=0.68 respectively
E) Heatmap of normalized change in correlation for thresholded pairs across timescales (bin sizes) and significance thresholds (p-values) in FC mice. Red: increase in correlation across days, Blue: decrease across days, white: no change.
F) Normalized change in correlations for thresholded cell pairs across significance levels. A bin size of 1.7 seconds was used. LME Group X Population interaction. E/E X FC and E/N x FC interactions p = 0.65 and p=0.68 respectively
G) Heatmap of normalized change in correlation for thresholded pairs across timescales (bin sizes) and significance thresholds (p-values) in HC mice. Red: increase in correlation across days, Blue: decrease across days, white: no change

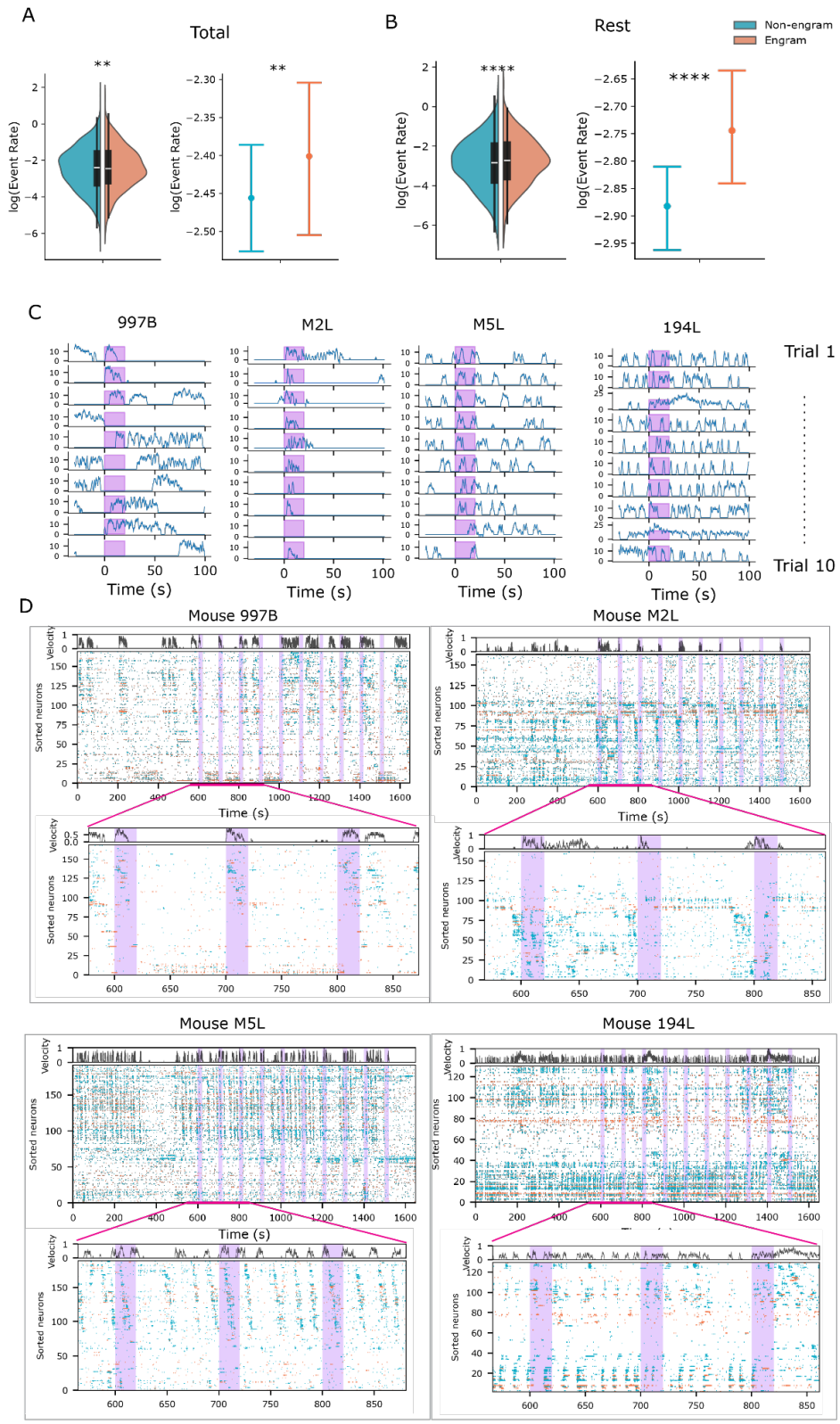
A
Total
B
Rest
Non-engram
Engram
log(Event Rate)
**
****
C
997B
M2L
M5L
194L
Trial 1
Trial 10
Time (s)
D
Mouse 997B
Mouse M2L
Mouse M5L
Mouse 194L
Velocity
Sorted neurons
Time (s)

1308

Supplementary Figure 7. Tone Recall Rates & Locomotion across trials.

A) Engram cell rates (log) during Recall session. Linear Mixed Effects Model, effect of Population p = 0.006. Error bars represent 95% CI.
B) Engram cell rates (log) during Recall session, Rest only. Linear Mixed Effects Model, effect of Population p = 2e-5. Error bars represent 95% CI.
C) 4 example mice running behavior across trials. Trials 1-10 are shown from top to bottom, and tone period is shown in purple.
D) Additional rastermap-sorted raster plots for example mice (n=4). Beneath each raster is a zoomed inset of the first 3 trials (pink lines). Top: normalized velocity trace. Orange: engram cell calcium events, teal: non-engram cell calcium events. Purple: CS presentation

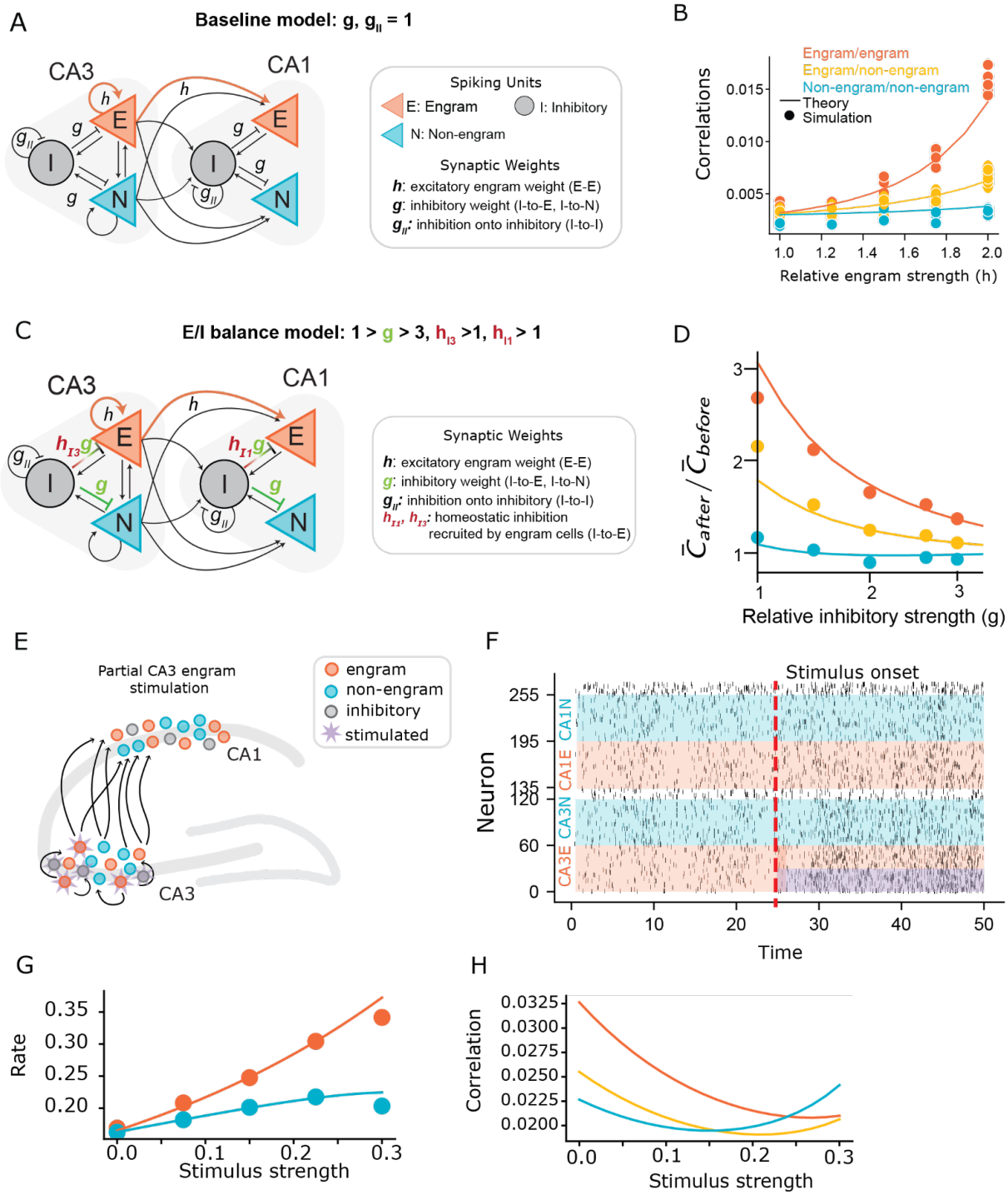
A
Baseline model: g, g_II = 1
CA3
CA1
Spiking Units
E: Engram
I: Inhibitory
N: Non-engram
Synaptic Weights
h: excitatory engram weight (E-E)
g: inhibitory weight (I-to-E, I-to-N)
g_II: inhibition onto inhibitory (I-to-I)
B
Engram/engram
Engram/non-engram
Non-engram/non-engram
Theory
Simulation
Correlations
Relative engram strength (h)
C
E/I balance model: 1 > g > 3, h_I3 >1, h_I1 > 1
Synaptic Weights
h: excitatory engram weight (E-E)
g: inhibitory weight (I-to-E, I-to-N)
g_II: inhibition onto inhibitory (I-to-I)
h_I1, h_I3: homeostatic inhibition recruited by engram cells (I-to-E)
D
Relative inhibitory strength (g)
E
Partial CA3 engram stimulation
engram
non-engram
inhibitory
stimulated
CA1
CA3
F
Stimulus onset
Neuron
CA1N
CA1E
CA3N
CA3E
Time
G
Rate
Stimulus strength
H
Correlation
Stimulus strength

1323

Supplementary Figure 8. Engram Model Simulations

A) Schematic representation of model. A subset of cells are engram cells with excitatory weights specified by *h*. Inhibitory connections are specified by *g*, and inhibitory weights onto engram cells are scaled with h_{I3} *or* h_{I1} for CA3 and CA1 respectively.

B) In our baseline model, where inhibition and excitation have the same relative strength, correlations of engram cells (orange lines) increase a large amount as a function of engram strength *h.*

C) Schematic representation of model with increased inhibition (E/I balance model). We introduced new parameters for homeostatic inhibition, hI3 and hI1, onto engram cells in addition to stronger global, non-specific inhibition (g > 1).

D) Introducing homeostatic and global inhibition (strong E/I balance) dampens correlations in engram population. The ratio of correlations after potentiation of engram weights (h = 2) to before (h = 1) as a function of baseline inhibition *g*.

E) Cartoon of stimulation procedure. A subset of excitatory Engram cells in CA3 received stimulation.

F) Raster plot to test engram reactivation in the model. A subpopulation of CA3 engram cells received stimulation (time 25) reactivation.

G) Stimulating a portion of the CA3 engram cells paired with disinhibition (an inhibitory input to the CA1, CA3 inhibitory cells) leads to an increase in both CA1 engram rates and non-engram rates.

H) Stimulating a portion of the CA3 engram cells paired with disinhibition leads to a decrease in pairwise correlation across all populations.